ANL/NSE-21/66

MOSCATO Solver Development and Integration Plan

Nuclear Science and Engineering Division
Chemical and Fuel Cycle Technologies Division

About Argonne National Laboratory

Argonne is a U.S. Department of Energy laboratory managed by UChicago Argonne, LLC under contract DE-AC02-06CH11357. The Laboratory's main facility is outside Chicago, at 9700 South Cass Avenue, Argonne, Illinois 60439. For information about Argonne and its pioneering science and technology programs, see www.anl.gov.

DOCUMENT AVAILABILITY

Online Access: U.S. Department of Energy (DOE) reports produced after 1991 and a growing number of pre-1991 documents are available free at OSTI.GOV (http://www.osti.gov/), a service of the US Dept. of Energy's Office of Scientific and Technical Information.

Reports not in digital format may be purchased by the public from the National Technical Information Service (NTIS):

U.S. Department of Commerce
National Technical Information Service
5301 Shawnee Rd
Alexandria, VA 22312
www.ntis.gov
Phone: (800) 553-NTIS (6847) or (703) 605-6000
Fax: (703) 605-6900
Email: **orders@ntis.gov**

Reports not in digital format are available to DOE and DOE contractors from the Office of Scientific and Technical Information (OSTI):

U.S. Department of Energy
Office of Scientific and Technical Information
P.O. Box 62
Oak Ridge, TN 37831-0062
www.osti.gov
Phone: (865) 576-8401
Fax: (865) 576-5728
Email: **reports@osti.gov**

Disclaimer

This report was prepared as an account of work sponsored by an agency of the United States Government. Neither the United States Government nor any agency thereof, nor UChicago Argonne, LLC, nor any of their employees or officers, makes any warranty, express or implied, or assumes any legal liability or responsibility for the accuracy, completeness, or usefulness of any information, apparatus, product, or process disclosed, or represents that its use would not infringe privately owned rights. Reference herein to any specific commercial product, process, or service by trade name, trademark, manufacturer, or otherwise, does not necessarily constitute or imply its endorsement, recommendation, or favoring by the United States Government or any agency thereof. The views and opinions of document authors expressed herein do not necessarily state or reflect those of the United States Government or any agency thereof, Argonne National Laboratory, or UChicago Argonne, LLC.

ANL/NSE-21/66

MOSCATO Solver Development and Integration Plan

---

prepared by
Haomin Yuan
Nuclear Science and Engineering Division, Argonne National Laboratory

Nathaniel Hoyt
Chemical and Fuel Cycle Technologies Division, Argonne National Laboratory

Sep 30th 2021

Contents

List of Figures

List of Tables

Abstract

During FY21, we conducted ongoing development work for the MOSCATO (Molten Salt Chemistry and Transport) solver. The code development work primarily consisted of transitioning capabilities from the original version of the solver, which was written in OpenFOAM, into Nek5000. In doing so, a fast, highly parallelizable solver was created that is capable of complex chemistry and corrosion simulations for engineering-scale molten salt systems. The Nek5000 version of MOSCATO is now fully featured and capable of higher-fidelity simulations than were previously possible. Demonstration cases including a thermal convection loop have been simulated to test these new capabilities.

Although capable of large-scale simulations, MOSCATO is not well-suited to parametric studies of complete reactor geometries. These types of simulations are instead better handled by reduced-order modeling codes such as ORNL's Mole code. Reduced-order simulation tools like Mole, however, are dependent on high fidelity correlations to account for complex, coupled three-dimensional phenomena that they do not directly simulate. Tools such as MOSCATO must therefore be used to create these correlations, as suitable empirical relationships are not available for most molten salt systems. Toward that end, we used the Nek-derived version of MOSCATO to create new mass transfer correlations for three relevant cases including tubular, tube bank, and subchannel geometries. These new correlations are more accurate than any existing ones and can be readily integrated into any reduced-order modeling tools that are targeting full-scale MSR simulations.

1. Introduction

Molten salt reactors (MSR) are a promising candidate technology for next generation nuclear power plants. Their early development history has been comprehensively reviewed by MacPherson [1]. MSRs have received renewed recent interest due to their intrinsic safety features and sustainability; these features make MSRs one of the more promising Gen-IV nuclear designs. Efforts to develop the technology have been pursued globally at national laboratories and a variety of corporate entities, including several start-up companies [2].

While there are variants in which the molten salt is used exclusively as a coolant [3], most MSR designs have the actinides and other fission product species dissolved in the salt. This fuel salt can then be pumped in and out of the core to facilitate removal of the generated energy by an appropriate heat exchanger. Compared to the water used in BWRs and PWRs, the thermophysical properties of molten salts allow these reactors to run at higher temperatures with higher thermal efficiencies. Furthermore, the primary and secondary coolant loops operate at low pressures, which increases safety and lowers the overall capital cost. In an MSR system, the molten fuel salt contains actinide and fission product species within an alkali metal or alkaline earth halide salt mixture, which can be chloride or fluoride based. The mass transfer of species within the salt is important because the core reactivity is dictated by the quantities and spatial distributions of the fuel and fission products within the reactor. Local concentrations of species also dictate the thermophysical properties such as viscosity, thermal conductivity, and heat capacity that control the thermal hydraulic behavior of the reactor. All MSR designs must therefore consider the mass transfer behavior of the salt.

The fission products and impurities in the salt cause chemical and electrochemical reactions that result in corrosion of the reactor's structural materials. In the Molten Salt Reactor Experiment (MSRE, [1,4]), corrosion on the surfaces of the structural alloys was observed. Chromium depletion in the Fe-Cr-Ni alloy system can occur via oxidation at the salt-alloy interface with subsequent removal of chromium from the alloy, leaving a depleted zone as shown in Figure 1 [4]. In the solid fuel MSR designs, the oxidation of Cr in the alloy is usually initiated by impurities or other oxidizing agents that result from oxygen and moisture interactions. However, in liquid fuel MSR designs, additional corrosion pathways arise due to the increasingly oxidizing conditions that result from the altered fluoride balance during fission. Additionally, the radionuclides generated from the fission reactions deposit on the alloy surfaces in liquid fueled MSRs, further altering the dynamics and spatial distribution of the corrosion processes.

Predictions of the local rates of these chemical and corrosion processes are crucial because the degradation of the structural alloys can ultimately determine the achievable lifetime of the molten salt equipment. Beyond corrosion, tracking of the fission products is also essential to ensure proper nuclear material accountancy. As such, corrosion and radionuclide deposition modeling require careful tracking of the transport of chemical species both within the salt and within the alloy. Early attempts to perform modeling were dependent on simple mass transfer coefficients, such as the work done by Kedl [5]. In this work, a constant coefficient was employed to account for mass transfer because computational approaches were deemed too expensive given the available computational resources during the 1970s. Due to the vast increase in computational resources since then, simplifications such as this are no longer required and high-fidelity computational fluid dynamics (CFD) simulations can instead be performed.

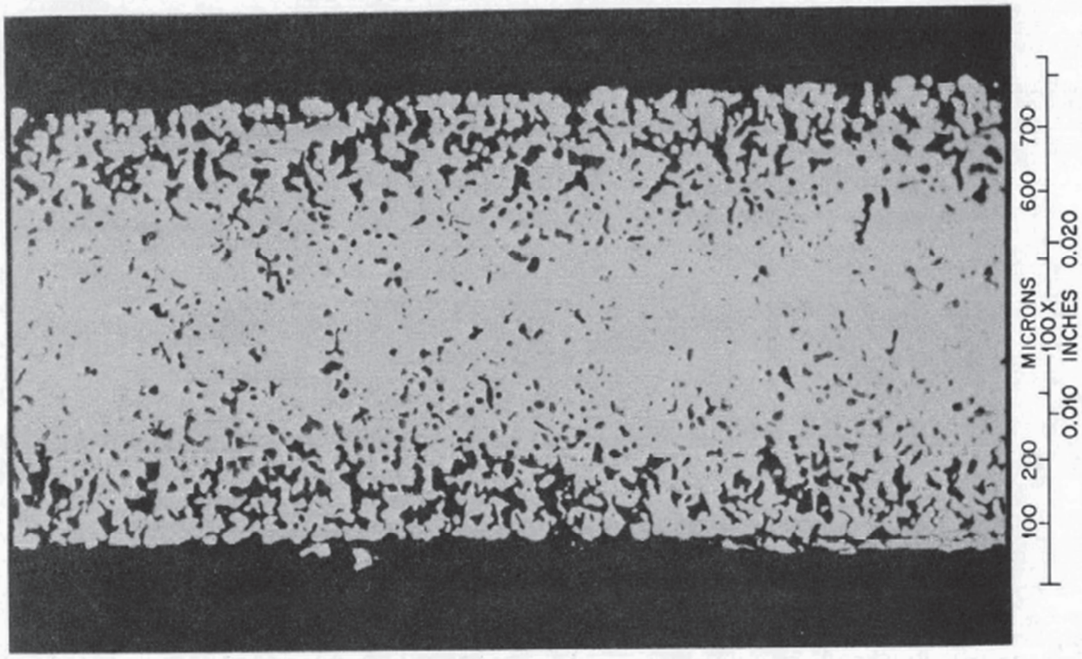

Fig. 6. Type 304L Stainless Steel Specimen from Loop 1258 Exposed to LiF-BeF$_2$-ZrF$_4$-ThF$_4$-UF$_4$ (70-23-5-1-1 mole %) for 45,724 hr at 685°C.

Figure 1 Typical alloy corrosion from molten salt interaction [6]

The development of the **MO**lten **S**alt **C**hemistry **A**nd **T**ransp**O**rt (MOSCATO) code at Argonne seeks to address this need. Three principal parts are ultimately needed to properly model the chemistry and corrosion in molten salt systems. First, mass transfer equations must be coupled with the Navier-Stokes (NS) equations in order to account for the transport of ion species in the salt. To model the transport of ions, the Poisson-Nernst-Planck (PNP) equation is used. Second, the diffusion of alloy constituents such as Cr and Fe must be simulated within the structural metals. The length scale of the alloy depletion layers is on the order of micrometers, which means the numerical domain for simulations of the alloy is much smaller than the fluid domain. Third, the alloy and salt domains must be coupled using models that account for the chemical and electrochemical reactions that occur at the salt-alloy interface. The local reaction rates are governed by kinetics equations such as the Butler-Volmer equation [7]; however, the coupling cannot simply be local. Instead, the salt and alloy regions must be globally coupled to account for charge conservation across the entire domain.

The coupled non-linear systems that arise involve multiple phenomena, multiple time-scales, and multiple domains. As such, it can be a considerable challenge to achieve successful simulations of these complex systems. However, through careful selection of numerical methods and coupling of the segregated solvers, MOSCATO is able to readily simulate these complex multiphysics scenarios. Details of the MOSCATO solver and the types of results that it can achieve are included in the sections below. Section 2 describes the numerical methods and modeling approach used by MOSCATO, while Section 3 shows the results from demonstration cases. These demonstration cases include results from simulations of a full-scale thermal convection loop. Section 4 describes the results of component-level simulations using MOSCATO; these results can be readily analyzed and distilled into a form suitable for integration into reduced-order MSR simulation tools. Section 5 then describes conclusions and the planned work for FY22.

2. Numerical Methods and Molten Salt Chemistry Modeling

2.1 Molten Salt Chemistry and Transport

Simulations of the chemistry and corrosion in molten salt systems is extremely complex. Any suitable molten salt chemistry solver must account for the transport of ions in the salt, the diffusion of species within the structural alloys, heterogeneous reaction kinetics at the salt-alloy interface, homogeneous reaction kinetics in the salt, and globally coupled charge-transfer characteristics. These coupled phenomena occur over multiple length and time scales, making their solution challenging. The MOSCATO solver uses a segregated approach to simultaneously solve for all of the phenomena. A description of the overall models and solution algorithm are included below. Additional details of the underlying solver also appeared in earlier technical reports.

Transport of ions in the salt is described by the PNP equations. The PNP equations describe the time evolution of the concentrations of ion species ([8], [9]). They are derived by considering the conservation of mass in the context of chemical reactions, diffusion due to concentration gradient, and migration due to electric potential fields ([8], [9]). The salt solution is assumed electrically neutral, which is called electroneutrality, and it is strictly maintained in all solutions except in a thin double layer near electrodes and other boundaries ([7]). The phenomena at this double layer is taken into account through the use of electrode kinetics as a boundary condition.

$$\frac{\partial c_k}{\partial t} + u \cdot \nabla c_k = D_k \nabla^2 c_k + (z_k u_k F) \nabla \cdot c_k \nabla \phi$$

$$\sum_k z_k c_k = 0$$

Electroneutrality combined with the ion transport equation leads to the potential equation [7]. It is a Poisson equation, similar to the pressure equation that arises in split operator treatments of the Navier Stokes equations.

$$\sum_k z_k \frac{\partial c_k}{\partial t} = \sum_k z_k \left[D_k \nabla^2 c_k + (z_k u_k F) \nabla \cdot c_k \nabla \phi \right] = 0$$

The PNP equations for the salt species are ultimately solved in concert with the Navier-Stokes equations. Scaling considerations result in different mesh resolution requirements for the respective concentration and velocity fields. For example, when non-dimensionalized, the incompressible Navier-Stokes equations take the form.

$$\frac{\partial u}{\partial t} + u \cdot \nabla u = \frac{1}{\mathrm{Re}} \nabla^2 u - \nabla P$$

Ignoring the migration term, the non-dimensionalized form of the PNP equation takes the following form:

$$\frac{\partial c}{\partial t} + u \cdot \nabla c = \frac{1}{\mathrm{Re} \cdot \mathrm{Sc}} \nabla^2 c$$

These equations are similar in appearance, except for the presence of the term *Sc*, which is the Schmidt number. Here, $Sc = \nu / D = \mu / (\varrho D)$. This number is analogous to the Prandtl number in heat transfer. The Schmidt number represents a scaling factor that describes the thickness of concentration boundary layers compared to velocity boundary layers. For the ion species in molten salt media, the Schmidt number is on the order of 1000. This very high Schmidt number leads to very thin concentration boundary layers, and special techniques such as the Artificial Viscosity Model are needed to fully close this problem.

A variety of reactions can cause corrosion, and MOSCATO seeks to account for all of them. For example, depletion of chromium in Fe-Ni-Cr alloys in molten salt environments can occur from a number of oxidation-reduction reactions that result in the selective removal of chromium. Representative reactions are listed below. Some reactions are due to the impurities in the salt melt (i.e., interactions with FeF_2, NiF_2 or HF), while others may result from melt constituents such as UF_4 [4]:

$$FeF_2 + Cr^0 \leftrightarrow CrF_2 + Fe^0$$
$$NiF_2 + Cr^0 \leftrightarrow CrF_2 + Ni^0$$
$$2HF + Cr^0 \leftrightarrow CrF_2 + H_2$$
$$2UF_4 + Cr^0 \leftrightarrow 2UF_3 + CrF_2$$

All of these reactions occur simultaneously in any given molten salt system, and they all must be taken into account. To do so, each reaction can be generalized in terms of specific oxidation-reduction reactions governed by individual reaction kinetics. The rate of the chemical reactions in corrosion and radionuclide deposition model are determined by the electrode kinetics, along with the assumption that the total net current is zero everywhere. The rate of the chemical reactions determines the depletion of Cr in the alloy and the deposition of radionuclide. The rate of the chemical reactions is governed by Butler-Volmer equation [7], which is shown below.

$$i_n = i_0 \left\{ \exp\left[\frac{(1-\beta)\mathrm{nF}}{RT}\eta \right] - \exp\left[-\frac{\beta \mathrm{nF}}{RT}\eta \right] \right\}$$

Here η is the overpotential, and $\eta = E_{electrode} - E_{equilibrium}$. In the above definition, $E_{electrode}$ is the electrode potential and $E_{equilibrium}$ is the equilibrium potential. The equilibrium potential is defined in the following equation.

$$E_{equilibrium} = E^* + \frac{RT}{nF}\ln\left(\frac{c^{n+}}{c}\right)$$

Where c^{n+} is the ion molar concentration in salt and c is the element concentration in alloy. And E^* is the tabulated formal potential of this reaction. The electrode potential is a single value assuming all the parts are electrically connected. For corrosion cases, its value is not fixed but adjusts to whatever value is necessary to ensure that the total net current is zero. Therefore, the solver must find the correct $E_{electrode}$ value at every time step. Due to the non-linearity of this problem, Newton's method is used iteratively determine these correct $E_{electrode}$ values.

The rate of the chemical reactions is a function of many factors, such as temperature, local ion concentration in the salt, local element concentration in the alloy, etc. Therefore, in order to accurately calculate the rate of reactions, we must not only couple Navier Stokes equations and PNP equations, but also model the change of element concentrations in the alloy. shows the experimental results showing the element concentration in the alloy after long-term exposure to a fuel salt [4]. Due to thinness of the depletion layers, diffusion in the alloy can be assumed to be one-dimensional. This assumption was also adopted by ORNL [10]. However, ORNL's model was not coupled with CFD simulations but instead assumed uniform, one-dimensional flow within the salt with infinitely fast mass transfer to the salt-alloy interface.

The length scale of the alloy diffusion process is on the order of 10 to 100 micrometers, which is significantly smaller than the flow length scale. Therefore, it is unnecessary to explicitly mesh the alloy domain to solve the diffusion equation. Instead, for each grid point on the salt-alloy, the Nek5000 version of MOSCATO solves the one-dimensional diffusion equation in a user defined length by discretizing it. At the bulk end, Dirichlet boundary conditions are applied for each alloy constituent's concentration. At the salt-alloy interface, Neumann boundary conditions are adopted, using the flux determined by electrode kinetics. Therefore, by solving these diffusion equations, we can obtain the time history and profiles of species concentrations in alloy.

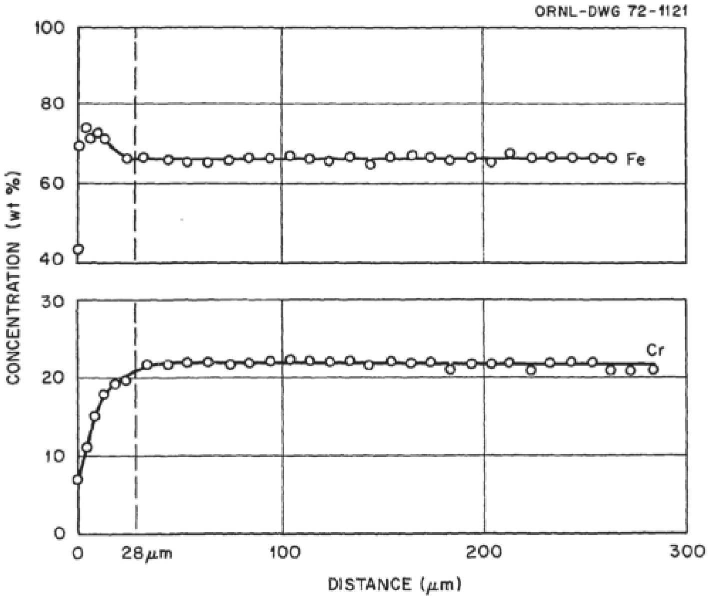

Fig. 27. Chromium and iron concentration gradient in a type 304L stainless steel specimen from loop 1258 exposed to LiF-BeF$_2$-ZrF$_4$-ThF$_4$-UF$_4$ (70-23-5-1-1 mole %) for 5700 hr at 688°C.

Figure 2 Profile of element concentration in alloy exposed to fuel salt [11]

2.2 Solver Implementation

The equations in Section 2.1 form a coupled system that must be solved in a consistent manner to achieve fast, reliable results. A number of different implementation approaches may be adopted to solve this system, each with different advantages and disadvantages. Development of the earliest form of MOSCATO solver began years ago using OpenFOAM. In its earliest form, this solver was used for simulations related to reprocessing of spent nuclear fuel [12]. Inclusion of thermogalvanic phenomena and other crucial corrosion behavior relevant to MSRs began in FY20 under the NEAMS Chemistry and Corrosion program.

OpenFOAM is an open-source finite volume modeling toolkit for solving partial and ordinary differential equations [13]. Due to its open-source nature, the original solver could be implemented by extending and adapting existing related solvers and libraries for compressible flow and multicomponent transport [14]. OpenFOAM is based on the Finite Volume Method (FVM). The computational domain is discretized into cells, which could be various types, such as tetrahedron, wedge, hexahedron, pyramids, polyhedron, etc. OpenFOAM was chosen initially due to is flexibility and its existing libraries that could be directly utilized. However, limitations also exist for OpenFOAM. The biggest bottleneck is its scalability for large problems. For example, the parallel performance drops significantly when there are less than 10,000 cells per cores.

Due to these limitations, transitioning of the MOSCATO solver to the Nek5000 platform was begun in late FY20. Nek5000 is based on the spectral-element method [15], which is a high-order weighted residual technique that combines the geometric flexibility of finite elements with the rapid convergence and tensor-product efficiencies of global spectral methods. Nek5000 solves the incompressible Navier-Stokes equations, with density variation is allowed through low-Mach approximation. Globally, the spectral-element method is based on a decomposition of the domain into smaller domains (elements), which are assumed to be curvilinear hexahedral elements that conform to the domain boundaries [16] [17]. Locally, functions within each element are expanded as Nth-order polynomials cast in tensor-product form. Temporal discretization is based on a high-order splitting that is third-order accurate in time and reduces the coupled velocity-pressure Stokes problem to four independent elliptic solves per time step: one for each velocity component and one for the pressure. The velocity problems are diagonally dominant and thus easily solved by using Jacobi preconditioned conjugate gradient iteration. The pressure sub-step requires a Poisson solver at each step, which is affected through multigrid-preconditioned GMRES iteration coupled with temporal projection to find an optimal initial guess. Particularly important components of Nek5000 are its scalable coarse-grid solvers that are central to parallel multigrid [18]. The subgrid-scale model employed relies on explicit filtering [18]–[21]. Nek5000 has been successfully applied to large-scale high-fidelity simulations for many nuclear components, such as random pebble bed, wire-wrapped fuel pins rod bundle. These cases have millions of elements, which leads to billions of degrees of freedom.

The development and use of the Nek5000 version of MOSCATO has enabled molten salt chemistry simulations with far greater fidelity that what had been achievable in the past. Even greater performance is possible using the latest Nek development – NekRS. NekRS [22] is a GPU variant of Nek5000 that has been greatly restructured with C++/OCCA code. The performant kernels in NekRS started as an early form from libParanumal ([23], [24]) and were tailored and expanded to meet the specific requirement of large-scale turbulence flow applications in complex domains [22]. NekRS also provides access to the standard Nek5000 interface and features, which allows users to leverage existing application-specific source code and data files on GPU-based platform [22]. Given the higher performance and relative ease of updating the existing codebase to NekRS, effort is now being devoted to make a final updated version of MOSCATO within the NekRS framework. This final version will serve to provide unparalleled high-resolution multiphysics studies of the complex chemistry and corrosion phenomena that occur in molten salt equipment.

3. MOSCATO-Nek5000 Demonstration Cases

The Nek5000 version of MOSCATO was tested using a variety of demonstration cases to assess the solver's performance. Two particular test cases are discussed below. The first involves a demonstration of a corrosion of a simple two-dimensional enclosure caused by FeF_2 impurities. The second case involved the simulation of a complete thermal convection loop.

3.1 Two-dimensional Impurity-Driven Corrosion Demonstration Case

The first example problem we present is the corrosion cavity. The numerical domain is inspired by reference ([25]). However, the problem of interest was the impurity-driven corrosion of a Cr-containing alloy caused by FeF_2 impurities in the salt. The salt was set to be quiescent, which thereby causes the rate of corrosion processes to become controlled by diffusion in the salt.

For this case, we adopted the parameters from Wetzel [10], which are shown in Table 1. The problem used a linear kinetic description for the reactions at the salt-alloy interface. This kinetic relationship took the form $i_n = i_0\eta$. For this case, we set $i_0 = 1\times10^{-3}$ A/V. The numerical domain is a two-dimensional square, with length of 1mm, and the mesh used in this case is shown in Figure 3. There are 100 elements in total, with polynomial order of seven, making the total Degrees of Freedom (DOF) equal to 34300.

Table 1 Initial conditions and parameters for corrosion model

Parameters	Values
c_{Cr2+}	1.928 mol/m^3
c_{Fe2+}	5.685 mol/m^3
c_{Cl-}	15.226 mol/m^3
c_{Cr}	24217 mol/m^3
c_{Fe}	101466 mol/m^3
D_{Cr2+}	1.1e-9 m^2/s
D_{Fe2+}	1.1e-9 m^2/s
D_{Cl-}	2.5e-9 m^2/s
D_{Cr}	4.2e-19 m^2/s
E^*_{Cr}	-3.28 V
E^*_{Fe}	-2.92 V
$k_{0\ Cr}$	2.17e-10 /s-cm^2
$k_{0\ \mathrm{Fe}}$	5.77e-9 /s-cm^2
α_{Cr}	0.32
α_{Fe}	0.09
F	96485.33 C/mol
R	8.3145 J/mol-K

This test case was chosen as it provides a suitable demonstration of a corrosion scenario with multiple dissolved ion species whose rates of oxidation and reduction are dictated by global charge conservation considerations. Figures 4 and 5 show the contours of Cr^{2+} and Fe^{2+} in the salt at different times during this simulation. The range of the figures' legends is changed for data at different times. As expected, Cr^{2+} slowly increases due to positive flux at wall, while Fe^{2+} is removed from the salt. Figure 6 shows the resulting profile of Cr in the alloy at different times. As expected, Cr is increasingly depleted from the alloy. This simple case includes many of the corrosion phenomena of interest in full-scale molten salt equipment. The fact that the solver was able to rapidly generate the results provided confidence that it would be able to simulate far more challenging geometries and scenarios.

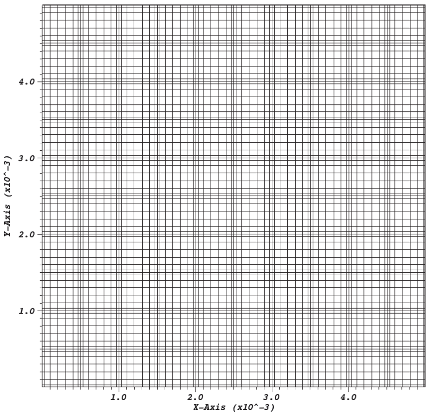

Figure 3 Mesh for corrosion cavity case

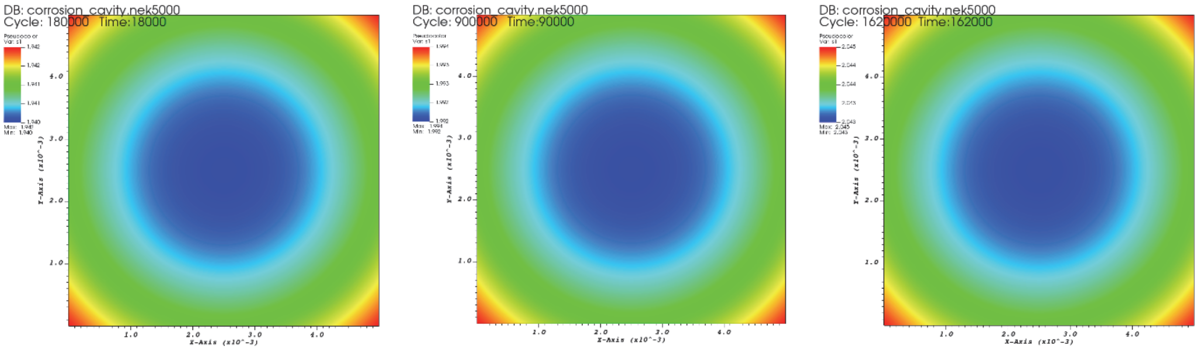

50hr 250hr 450hr

Figure 4 Profile of Cr^{2+} in the salt

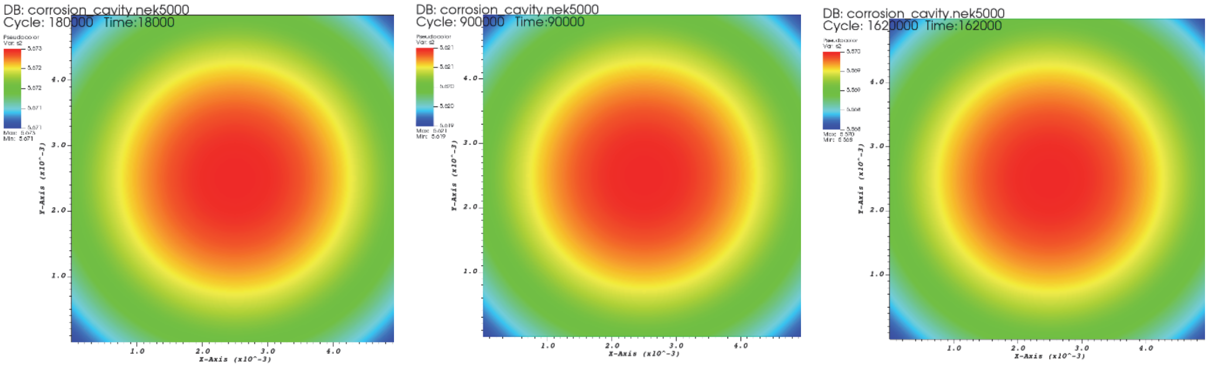

50hr 250hr 450hr

Figure 5 Profile of Fe^{2+} in the salt

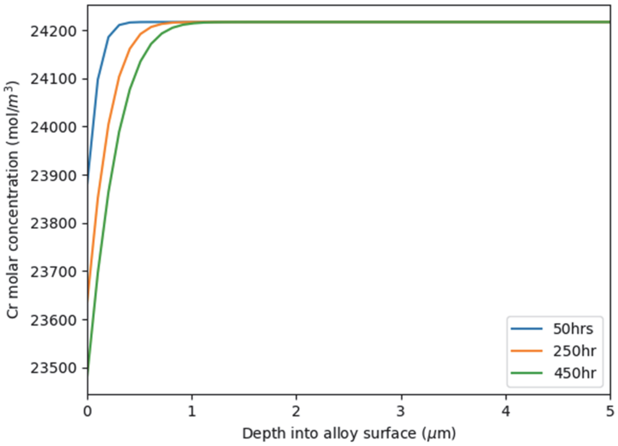

Figure 6 Profile of chromium concentration in the alloy during the impurity-driven corrosion process

3.2 Thermal Convection Loop Demonstration Case

As a part of molten salt reactor development, small-scale experimental loops ([6]) have been created to test natural circulation and corrosion in flowing molten salts. These loops are called Thermal Convection Loops (TCLs). In order to test the Nek5000 version of MOSCATO, we used a TCL experiment conducted at UW-Madison to demonstrate the developed corrosion modeling approach. Details of this experiment can be found in reference [26]. This experiment loop used FLiBe as the fluid. Thermophysical properties for FLiBe were obtained from reference [27] and presented in Table 2. Temperatures in Table 2 have units of degrees Celsius. Since the density is a linear function of temperature, the Boussinesq approximation was used to account for variation in the salt density.

The parameters in Table 1 were again used for the TCL case. Butler-Volmer kinetics were used at the salt-alloy interface, with i_0 for the reduction/oxidation reaction defined using the following equation:

$$i_0 = nFk_0 \left(c^{n+}\right)^{1-\alpha} c^{\alpha}$$

Here, k_0 is the reaction rate.

Table 2 FLiBe properties

Density (kg/m3)	2413.0 - 0.488*(T+273.15)
Viscosity (cp)	0.116*exp(3755.0/(T+273.15))
Heat Capacity (J/kg-K)	2386
Thermal conductivity (W-K/m)	1.1

An overview of this loop and the positions of heaters, coolers, and thermocouples are presented in Figure 7. There were in total four radiation heaters in the loop. Two air-convection coolers were installed the loop, however, only the one in top section was active during the experiment. A mesh for this loop was constructed that contained 70384 elements. To accelerate the simulation speed for the demonstration, we performed simulations at polynomials of six, which leads to total DOF of 15 million. Figure 8 shows the mesh used in this case. As mentioned, the mesh near the salt-alloy interface had to be extensively refined due to the high *Sc* number.

In this demonstration, we used the Case 1 scenario in reference [26], which means the total power applied at all heaters was 952 W. A uniform heat flux boundary condition was applied at heater surface. This is a reasonable approach, as the radiation heater generates a uniform heat flux. In the cooler, the same amount of power was extracted uniformly. In reality, the heat flux for the cooler is likely less uniform than the heater, but uniformity is a reasonable assumption for a demonstration case at this stage. The heating and cooling set up a natural circulation flow in the loop. Predicted contours of the velocity magnitude and temperature under these conditions are shown in .

For this case, we adopted Butler-Volmer electrode kinetics using the parameters from Wetzel [10]. The use of Newton's method to determine the correct electrode potential took around ten iterations at the first time-step, but then reduced to three iterations per time-step throughout the course of the simulation. Due to the time constraints, we did not run the case sufficiently long to reach a physical time of hours in the simulation. Also, to reduce the computational time, we first solved the velocity and temperature fields until they converged. We then froze the velocity and temperature in the simulation but continued to solve the PNP equations and corrosion models based on the frozen profiles of velocity and temperature. Figures 9 and 10 show the contours of Cr^{2+} and Fe^{2+} in the loop after 3 minutes (189s). We also present some zoomed-in views in Figure 11. At last, the electric potential in the salt is shown in Figure 12.

Overall, the results look exactly as expected. During this early phase of corrosion, the impurity-driven corrosion depletes Cr from the alloy everywhere regardless of the temperature. This can be seen in Figure 13, where the calculated Cr concentration profiles are shown as a function of depth into the alloy. We sampled the Cr concentration profile at two locations: the temperature maximum and the temperature minimum. The maximum was located at the end of heater, where there is the highest temperature in the loop. The minimum was the position just before the flow entered the heater, where there is the lowest temperature in the loop. The Cr concentration profile in the alloy at these two locations are shown in Figure 13. The difference is very subtle, but it is evident that the temperature maximum has a slightly higher corrosion rate than the minimum.

Once this initial corrosion phase passes and the concentration of the FeF_2 impurity is lowered, the combined Cr transfer phenomena will take over and Cr will start to be deposited at the cold leg instead of being depleted. The *Sc* numbers for both Fe^{2+} and Cr^{2+} in this case were 6167. As such, the profiles of Fe^{2+} and Cr^{2+} were slightly under-resolved, as can be seen in Figure 11. This is an expected outcome and will be resolved in the future work by adopting the Artificial Viscosity Model to account for near wall regions in high *Sc* flows.

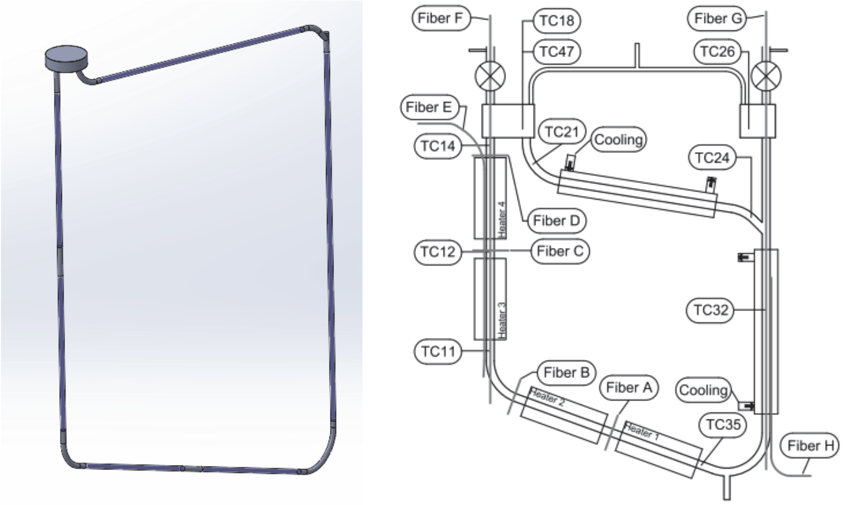

Figure 7 UW-Madison TCL loop (left) and heater, cooler, thermocouple position (right)

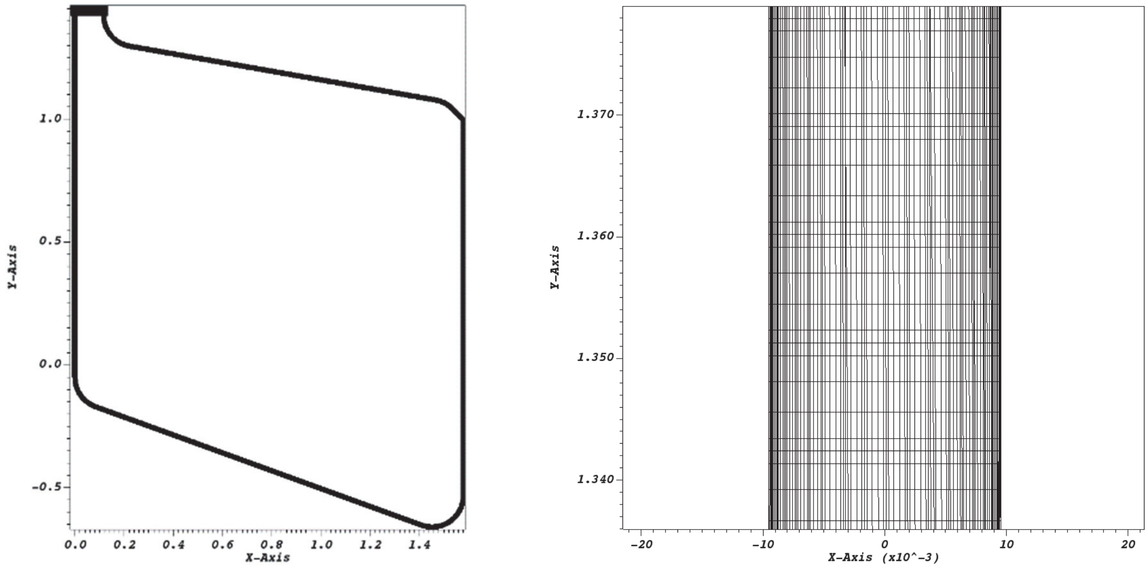

Overview *Typical mesh in heated tube section*

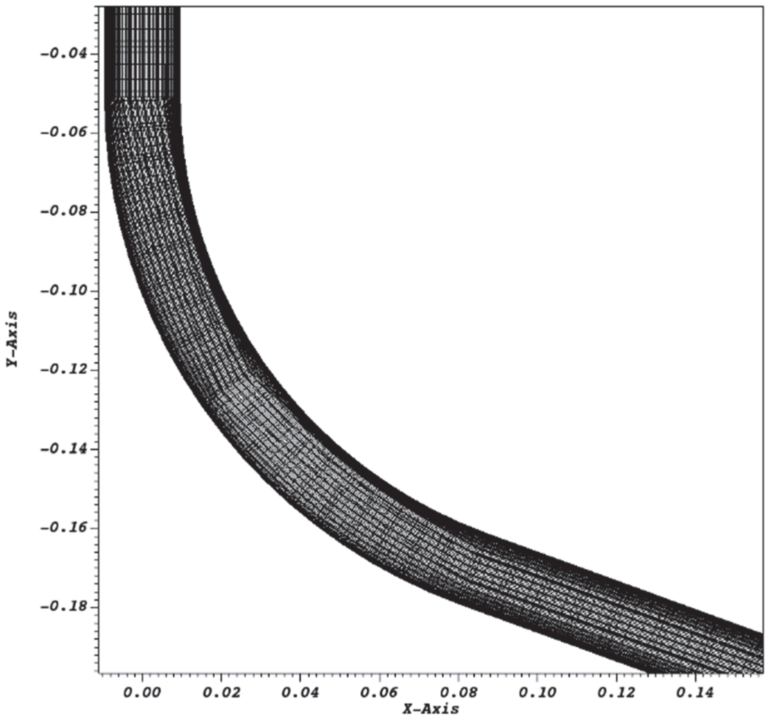

Mesh in bend

Figure 8 Mesh of UW-Madison TCL case

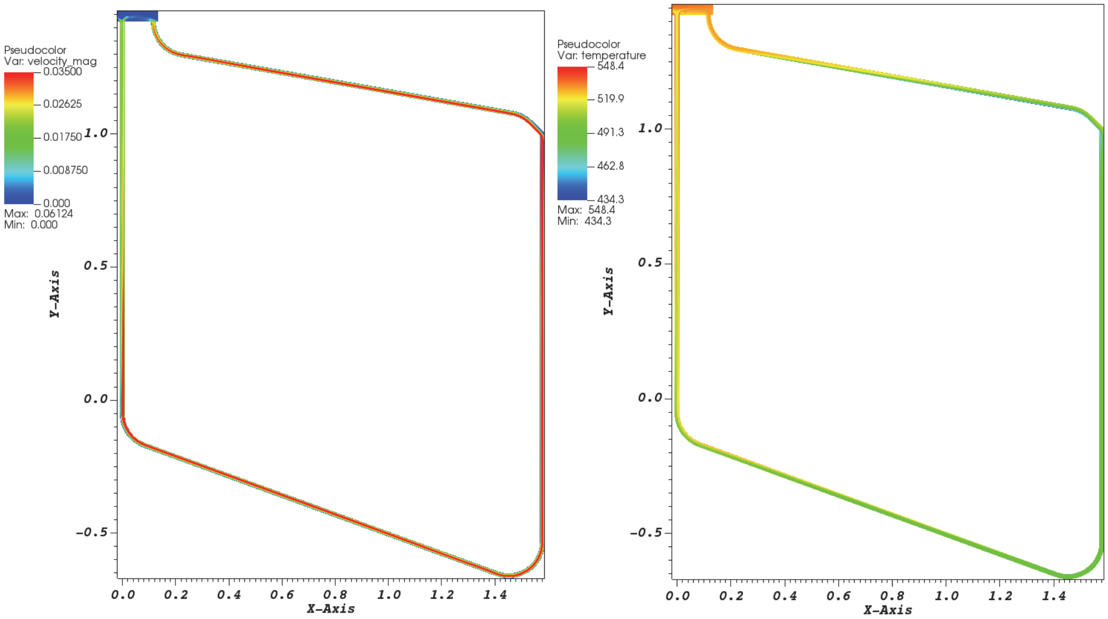

Figure 9 Velocity magnitude (left) and temperature (right) profiles in UW-Madison TCL

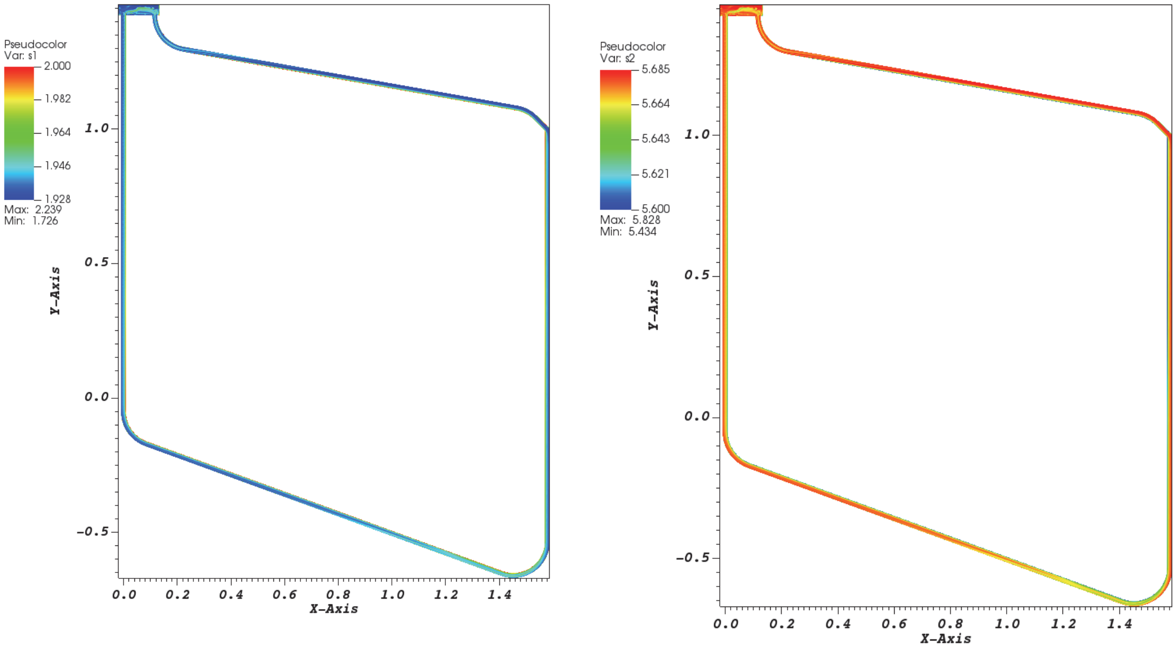

Figure 10 Cr^{2+} (left) and Fe^{2+} (right) molar concentration profile in TCL

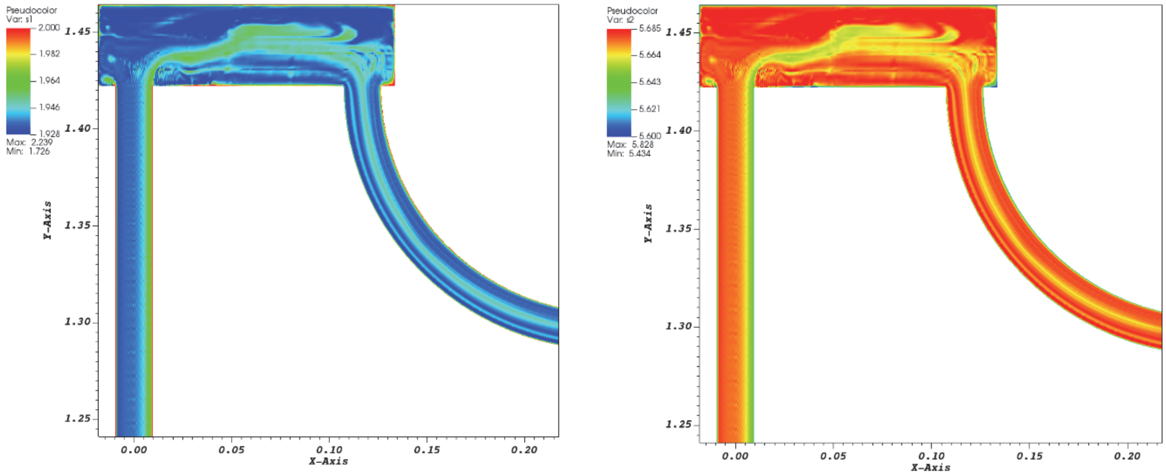

Cr^{2+} *profile* Fe^{2+} *profile*

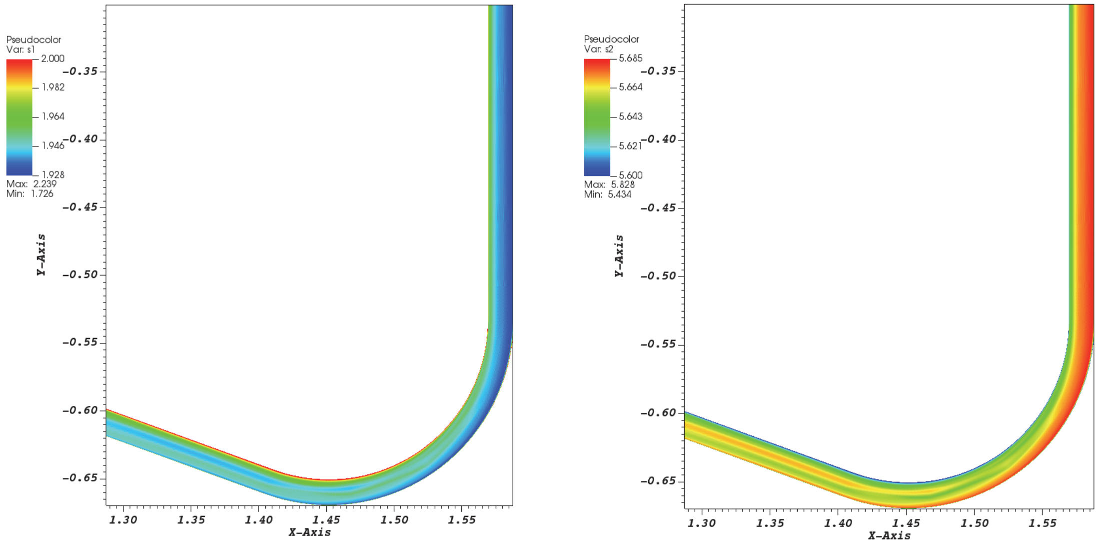

Cr^{2+} *profile* Fe^{2+} *profile*

Figure 11 Zoomed in view of molar concentration profile in TCL

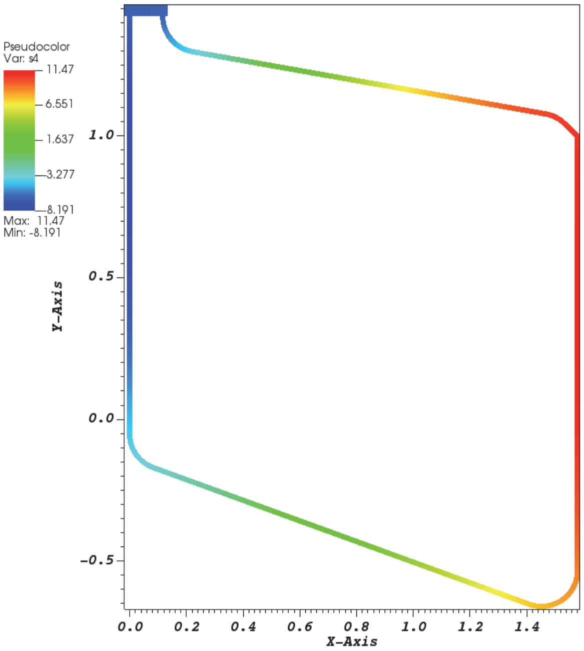

Figure 12 Electric potential in the salt

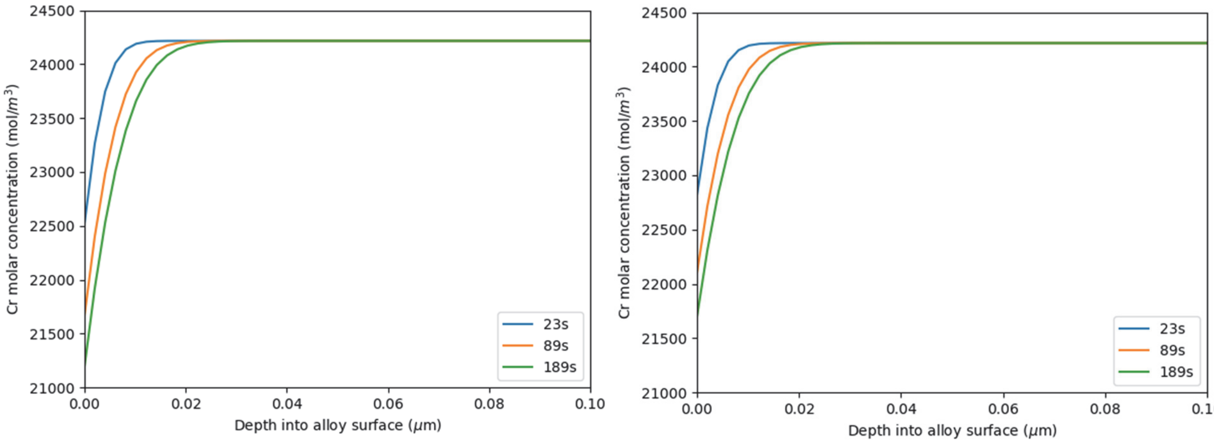

Hot point

Cold point

Figure 13 Chromium profile as a function of distance from the salt-alloy interface. Profile at the loops temperature maximum (left) and minimum (right)

4. Mass Transfer Relationships for Reduced-Order Solvers

Although MOSCATO is capable of full-scale simulations of molten salt systems such as flow loops, the computational expense for large-scale simulations is generally too large to conduct parametric design studies. As such, reduced-order solvers such as ORNL's Mole need to be used instead for this role. However, Mole is dependent on the use of a variety of chemical engineering correlations to describe phenomena such as the mass transfer of reactants to alloy surfaces. Although some of these correlations can be estimated using scaling laws and existing experimental results from aqueous media, bespoke correlations for molten salt behavior in geometries of interest to MSRs must be generated in order to ensure high-fidelity results. MOSCATO is particularly well suited to provide higher-order simulation results that can be distilled into satisfactory correlations. As such, this section describes the molten salt mass transfer correlations that were generated by MOSCATO for direct entry into the Mole framework.

4.1 Sherwood Number Correlation Simulations Using MOSCATO

Accurate mass transfer relationships are crucial for high-fidelity simulations of reaction rates using reduced-order models such as Mole. Most of the chemical phenomena of interest in MSRs, such as corrosion and fission product deposition, are ultimately controlled by the rate of mass transfer to the salt-alloy interface. Mass transfer in molten salt media is complicated because it falls into the category of high Schmidt number flow. The Schmidt number represents ratio between kinematic viscosity of the molten salt and the diffusivity of the ion species of interest (e.g., Cr^{2+}, Fe^{2+}, U^{3+}, etc.). The Schmidt numbers encountered in molten salts are as high as O(1000), which is usually two magnitudes higher than the Prandtl number. As such, the boundary layer for ion constituents near the salt-alloy interface is far thinner than either the momentum or temperature boundary layers. Direct simulations of mass transfer are therefore challenging as extremely high mesh resolutions must be present near the salt-alloy interface.

Studies of high Schmidt number flow has been going on for decades. Despite recent progress in modeling turbulence, simulating high Schmidt number flow is still a very challenging problem even for low Reynolds number flow. The Schmidt number for ion species in molten salt flow is O(1000), which means even for very low Reynolds number flow, we need a much higher mesh resolution for the concentration field to be fully resolved. The exchange of mass between a surface and a turbulent fluid at high *Sc* is also limited by a very thin boundary layer nested inside the viscous sublayer in which the mass transport is primarily molecular. The thickness of this concentration boundary layer (CBL) is denoted by δ_m^+ in reference[28], and from a classical prediction, we know that $\delta_m^+ \sim Sc^{-1/3}$[28]. Therefore, for *Sc*=1000, we need the first boundary layer thickness 1/10 of the boundary layer thickness designed for the *Re* number of the flow. This is very strict requirement that necessitates a need for increased resolution globally. The traditional approach to study high *Sc* flows is therefore similar to heat transfer analysis and is based on nondimensionalized correlations [29]–[31].

In the study of mass transfer, the Sherwood number (shown in the equation below) is used nondimensionalize the mass transfer rate. Due to the similarity of mass transfer and heat transfer, the Sherwood number is also called the mass transfer Nusselt number. It represents the ratio of the convective mass transfer to the rate of diffusive mass transport.

$$Sh = \frac{K}{D/L}$$

Here, *K* is the mass transfer coefficient, *D* is the diffusion coefficient of the species of interest, and *L* is a suitable length scale.

Mole and other reduced-order modeling approaches require accurate Sherwood number correlations to properly calculate the rate-controlling mass transfer behavior. Sherwood number correlations based on fits to experimental data are available; however, the correlations are typically limited to a small number of geometries and often must be extrapolated to reach a *Re* and *Sc* range relevant to molten salt systems. As performing molten salt experiments to generate valid correlations would be prohibitively expensive, computational fluid dynamics simulations of the salt chemistry provide a straightforward way to achieve the required correlations.

Computational fluid dynamic simulations to generate Sherwood numbers for high Schmidt number flow has been practiced for decades with varying degrees of success. One common approach is to employ RANS modeling along with a turbulent Schmidt number that is defined analogously to the turbulent Prandtl number [32], [33]. This approach is often successful; however, the turbulent Schmidt number various significantly (0.2-1.3) [32] for different applications, making this approach highly problem dependent. Another approach to is to use high-fidelity CFD technique, either Direct Numerical Simulation (DNS) or Large Eddy Simulation (LES). Most of the high-fidelity data (DNS/LES) reaches Schmidt number up to O (100) and for simple geometries, like channels or tubes [28], [34]–[36]. However, DNS or LES usually only resolve velocity components to a Kolmogorov scale or Taylor scale [37], but high Schmidt number flow requires resolution for a scale which is smaller still.

Beyond proper mesh resolution, none of the mass transfer studies properly account for migration in the salt. Migration is particularly important for highly concentrated species such as those encountered in MSRs. For these reasons, there is still a lack of high-fidelity data for higher Schmidt number flow in complex, relevant geometries. As such, we have used NekRS [22] to perform LES studies of high Schmidt number flows to provide Mole and other reduced-order solvers with the mass transfer correlations that they need.

4.2 Numerical Methods and Setup

The setup for the mass transfer correlation cases was similar to the demonstration cases considered in Section 3. However, for the cases in this section, the temperature field was assumed to be isothermal. To ensure flow is fully developed in the domain, triple periodicities were applied for all cases. To maintain the bulk flow rate constant, a dynamic force was applied uniformly in the stream-wise direction. The stream-wise direction periodicity will deplete the concentration in the domain. To avoid this depletion process, a mass source, which is a function of stream-wise velocity, was applied to the domain. This approach is analogous to adding a heat sink to the domain to achieve temperature stream-wise direction periodicity [38]. For the boundary conditions for concentrations, the simulated species were assumed to noble metal fission products with a concentration of zero at the salt-alloy interface. Additional complexity including non-isothermal conditions and concentration profiles dictated by chemical kinetics will be added as needed in FY22.

4.3 Sherwood Number Results

For FY21, we conducted simulations to provide mass transfer correlations for three MSR-relevant geometries. First, we considered flow in a simple tubular geometry. This case is representative of standard flow conduits used in MSRs. Second, a tube bank in cross flow was studied. This type of geometry is usually seen in the heat exchanger for nuclear power plants. Third, we studied the flow in subchannels of fuel assembly. This type of geometry is commonly seen in the core designs for some MSRs. The correlations generated for each of these geometries can be readily included in reduced-order solvers to allow them to have accurate predictions of molten salt mass transfer behavior.

4.3.1 Flow in straight tubular geometry

The first geometry simulated was a simple tubular section. The simulated geometry had a nondimensional diameter of 1.0, and a nondimensional length of 6.0. Figure 14 shows the mesh of this case. As we can see, the near wall mesh was extremely refined to meet the requirements to achieve satisfactory simulation for high Schmidt number fluids. The mesh contained 88200 elements. With polynomial order of 7, the total Degrees of Freedom (DOF) was more than 30 million. Two Reynolds numbers (3000,10000) and three Schmidt numbers (10, 50, 100) were simulated to generate the correlation. For each data point, data for more than five flow-through-times were collected to ensure convergence. Contours for the instantaneous velocity magnitude field are shown in Figure 15 for *Re* = 3000 and 10000. As expected, the flow field at *Re* = 10000 is much more turbulent than that at *Re* = 3000. Figure 16 presents the profile of concentration at *Re* = 3000 at various *Sc* number. Meanwhile, the same data but for *Re* = 10000 is shown in Figure 17. As we can see, for a fixed *Re*, as *Sc* increases the structure of concentration boundary layer gets smaller and requires more mesh resolution.

The Sherwood numbers generated by our computations can be compared with correlations available in the literature [39]. This correlation, shown below, is from the analysis of experimental results, but because it was developed for a broad range of *Re* and *Sc* and because it does not include migration, the results are expected to be different from our simulations. The direct comparisons of data from NekRS simulation and the literature correlation are shown in Figure 18. As we can see, data from correlation and simulation match reasonably well, which is expected for straight tube geometry.

$$Sh = 0.0102 Re^{0.9} Sc^{1/3}$$

Although the literature correlation for the tubular geometry was somewhat satisfactory, the mean relative error between the simulations and the correlation were 9.5%. Using the numerical results as a baseline, an alternate correlation more applicable to the molten salt system could be created. This new correlation is shown below.

$$Sh = 0.00308\, Re^{1.045}\, Sc^{0.327}$$

A comparison of this correlation to the numerical results is shown in Figure 18. With this new equation, the mean relative error between the simulated results and the correlation is now only 3.3%. As such, this improved correlation will be provided to Mole to account for mass transfer in the tubular geometry.

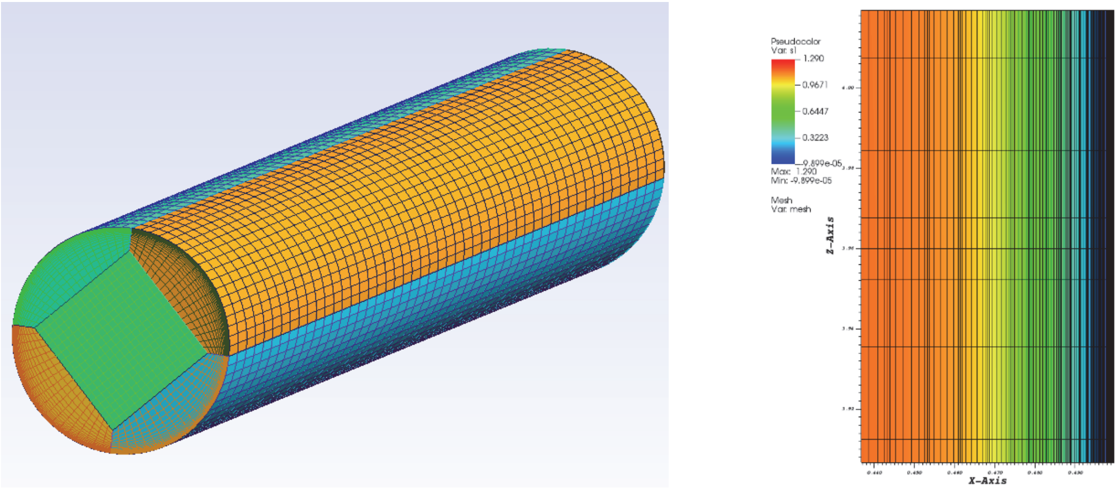

Figure 14 Mesh for tubular case (left: overview, right: near wall)

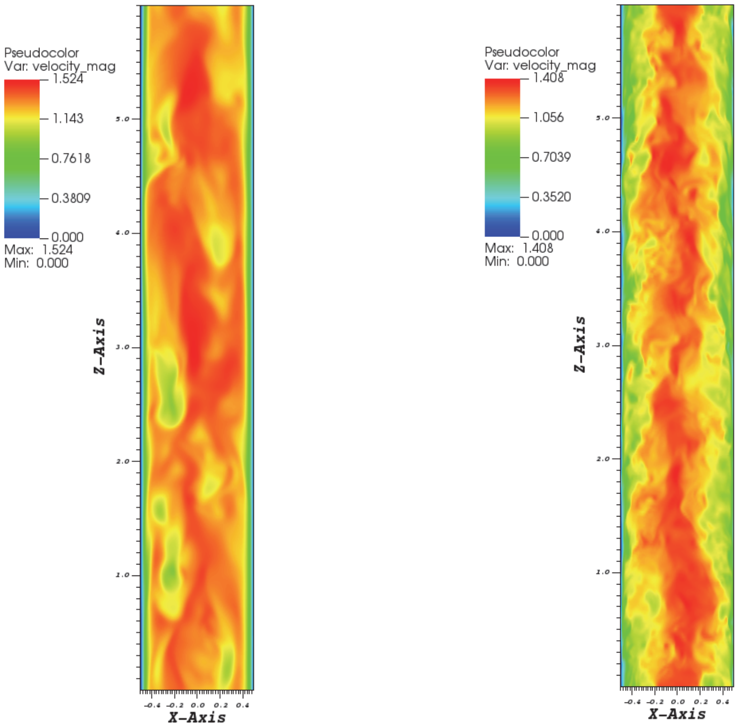

Figure 15 Instantaneous velocity magnitude in tube (left: Re=3000, Right: Re=10000)

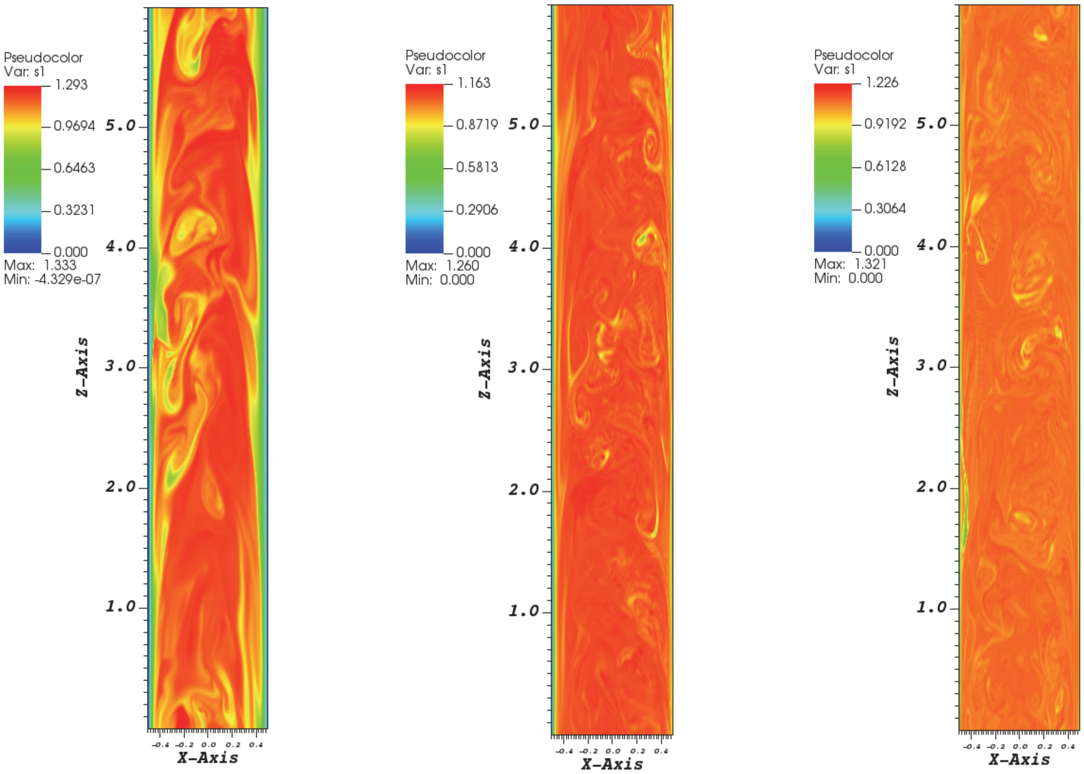

Figure 16 Instantaneous concentration field at Re=3000 (left: Sc=10, middle: Sc=50, right: Sc=100)

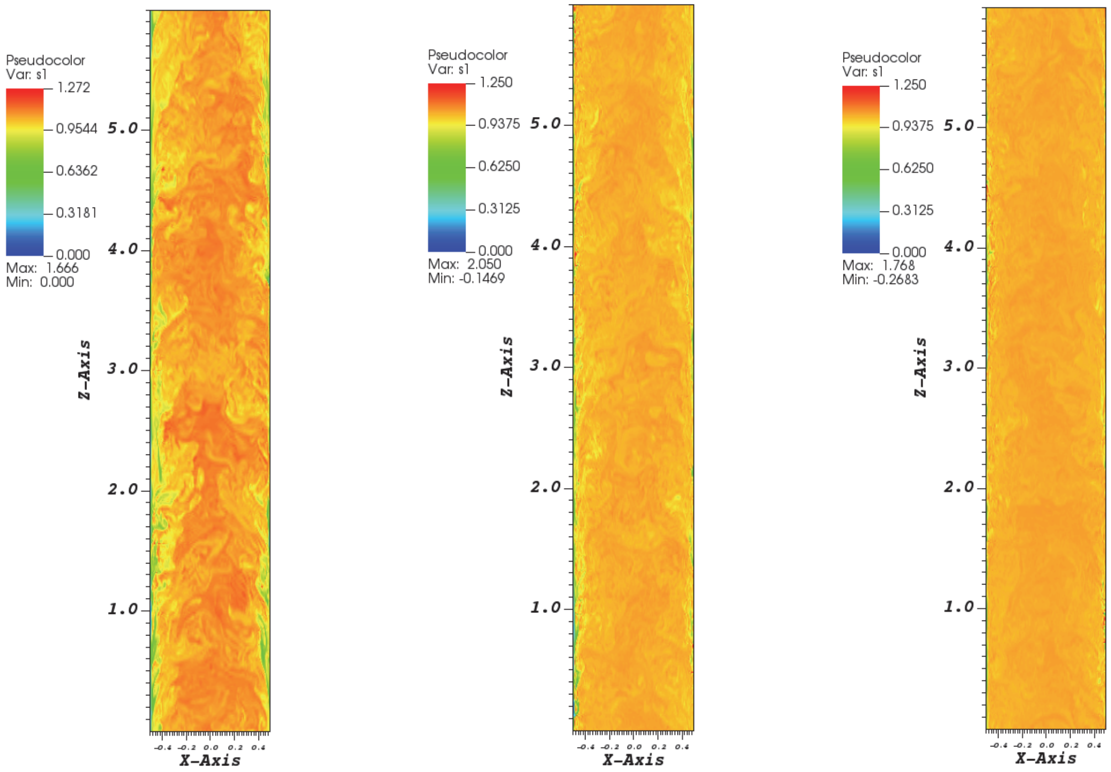

Figure 17 Instantaneous concentration field at Re=10000 (left: Sc=10, middle: Sc=50, right: Sc=100)

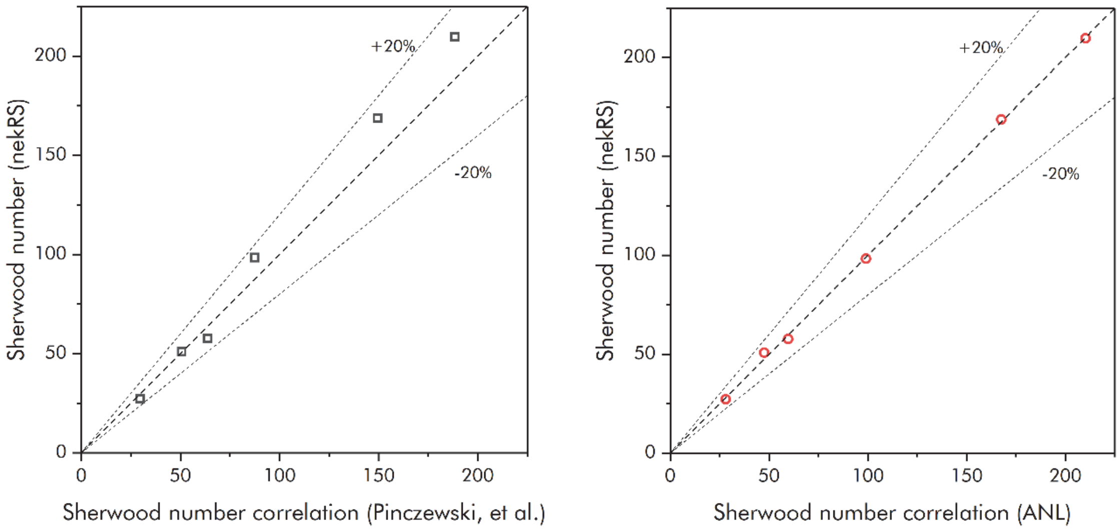

Figure 18 Comparison of Sherwood numbers obtained from NekRS simulations with existing correlation (left) and new correlation (right) for tubular geometry

4.3.2 Tube bank in cross flow

The second relevant geometry that we studied was an in-line tube bank in cross flow. This geometry is commonly encountered in MSR heat exchangers. Corrosion in heat exchangers is of particular importance due to the thin-walled structural materials located there. Nuclear material accountancy has also been extensively studies in these configurations. For this specific geometry, the nondimensional tube diameter was set to be 1.0, and the distance between tube centers was set to be 2.0. The domain geometry and mesh are shown in Figure 19. The mesh had 215040 elements with a polynomial order of seven, leading to more than 73 million total Degrees of Freedom (DOF).

Similar to the tube case, we also tested at two *Re* numbers and three *Sc* numbers. Figure 20 and Figure 21 present the instantaneous velocity magnitude field at $Re = 3821$ and 16042 respectively. Figure 22 through Figure 27 show the instantaneous concentration profiles at different *Re* and *Sc*. The trends are similar to what we observe in tube case.

For this case, we again compared the NekRS results with the correlation from literature [40]. This correlation, shown below, was originally developed for heat transfer, but it can be converted to a mass transfer correlation by analogy.

$$Sh = 0.34 F_a Re^{0.61} Sc^{0.31}$$

$$F_a = 1 + \left(\varphi_L + \frac{7.17}{\varphi_L} - 6.52\right) \cdot \left[\frac{0.266}{(\varphi_T - 0.8)^2} - 0.12\right] \cdot \sqrt{\frac{1000}{Re}}$$

Here φ_L and φ_T are dimensionless longitudinal and transverse pitch respectively. φ_L and φ_T are both equal to 2 in this case.

The comparison between data from NekRS simulation and the above correlation is shown in Figure 28. As can be seen, the trend is similar both datasets, namely *Sh* increases with increased *Re* and *Sc*. However, the correlation significantly underpredicts the mass transfer compared to simulations with a mean relative error of 18.8%, indicating a deficiency in the correlation. As such, the simulations were again used as a baseline to form a new correlation suitable for molten salt systems with the relevant range of Re and Sc. This new correlation is shown below.

$$Sh = 0.21 F_a Re^{0.66} Sc^{0.37}$$

Figure 28 shows the comparison between the simulated *Sh* values and the new correlation. In this case, the mean relative error between the correlations and the simulations is now only 1.0%. As such, this updated correlation will be provided to Mole to permit reduced-order simulations of the mass transfer for tube bank geometries.

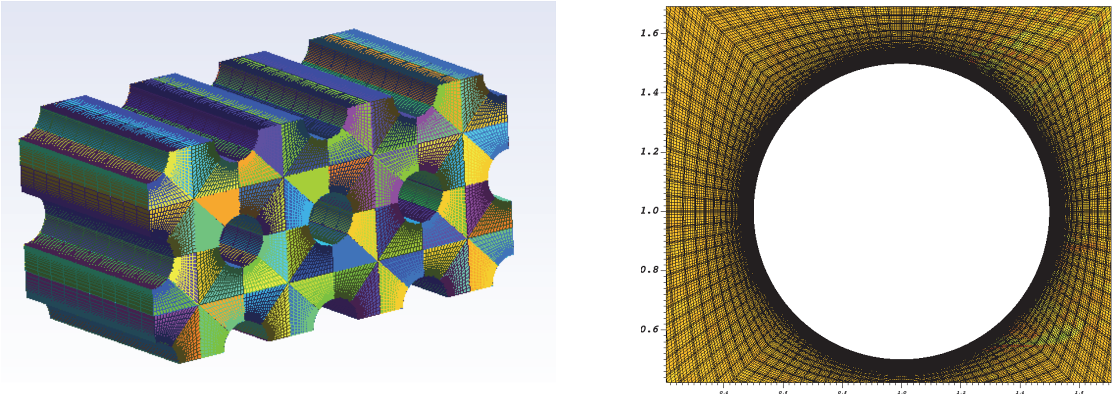

Figure 19 Mesh for tube bank cross flow case

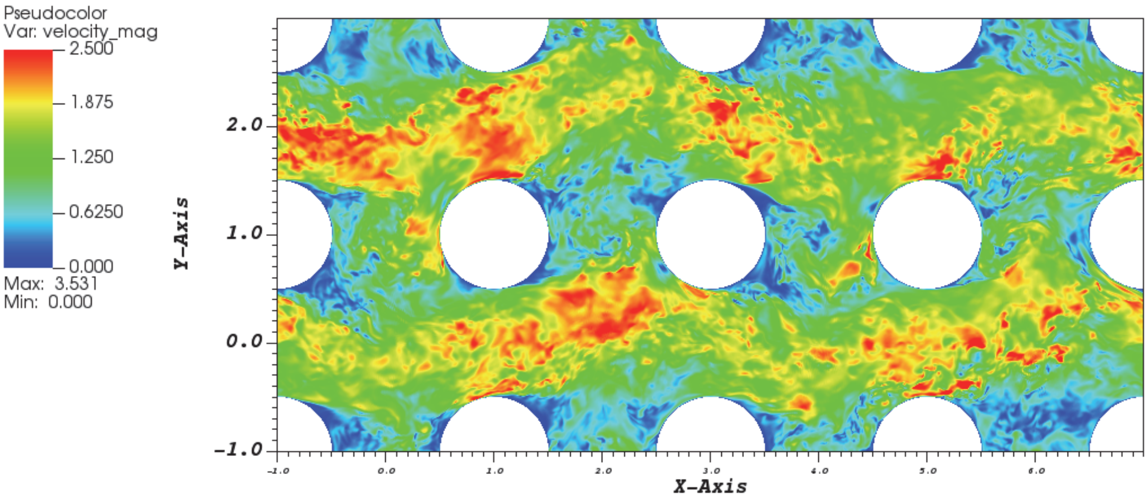

Figure 20 Instantaneous velocity magnitude field at Re=4821

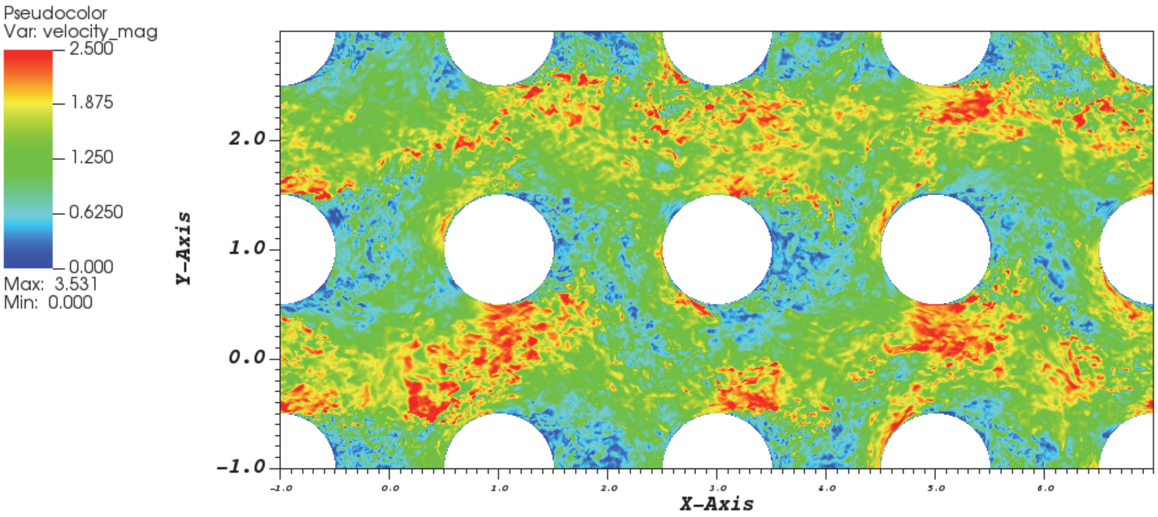

Figure 21 Instantaneous velocity magnitude field at Re=16042

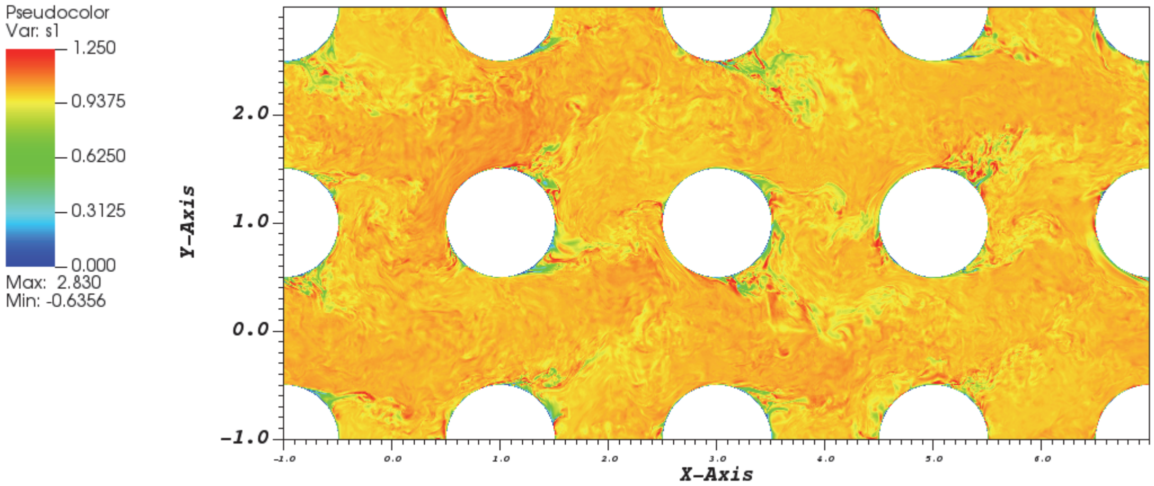

Figure 22 Instantaneous concentration field at Re=4821 Sc=10

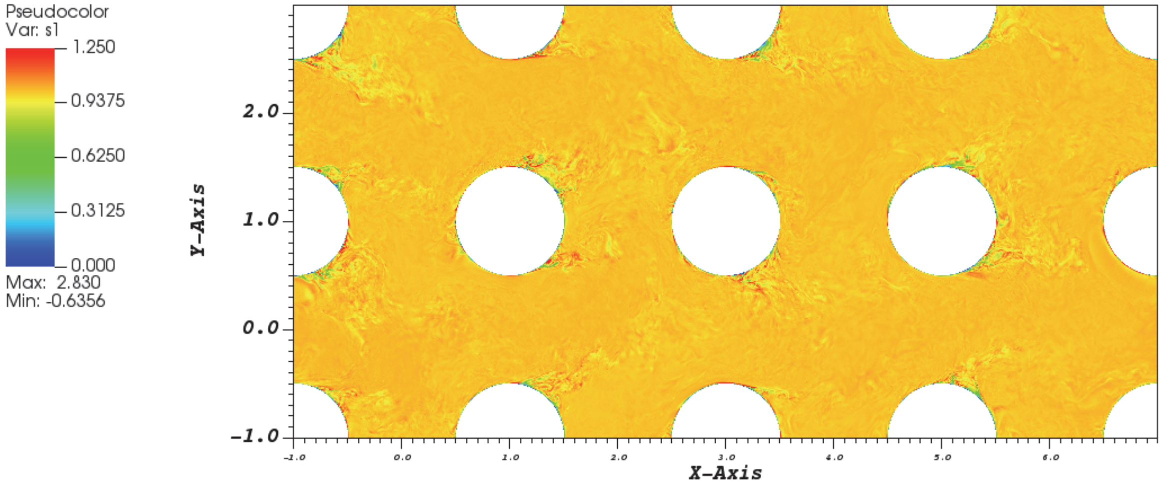

Figure 23 Instantaneous concentration field at Re=4821 Sc=50

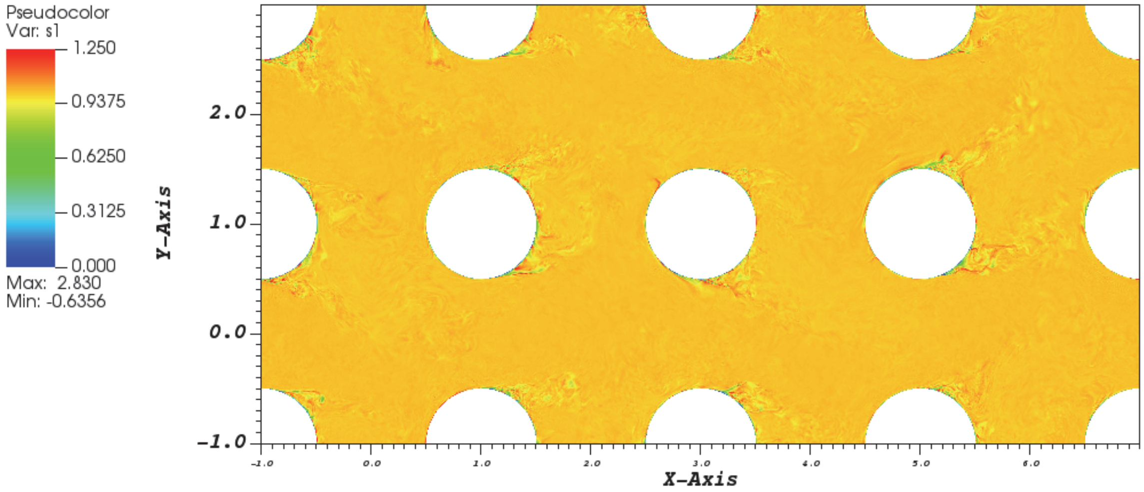

Figure 24 Instantaneous concentration field at Re=4821 Sc=100

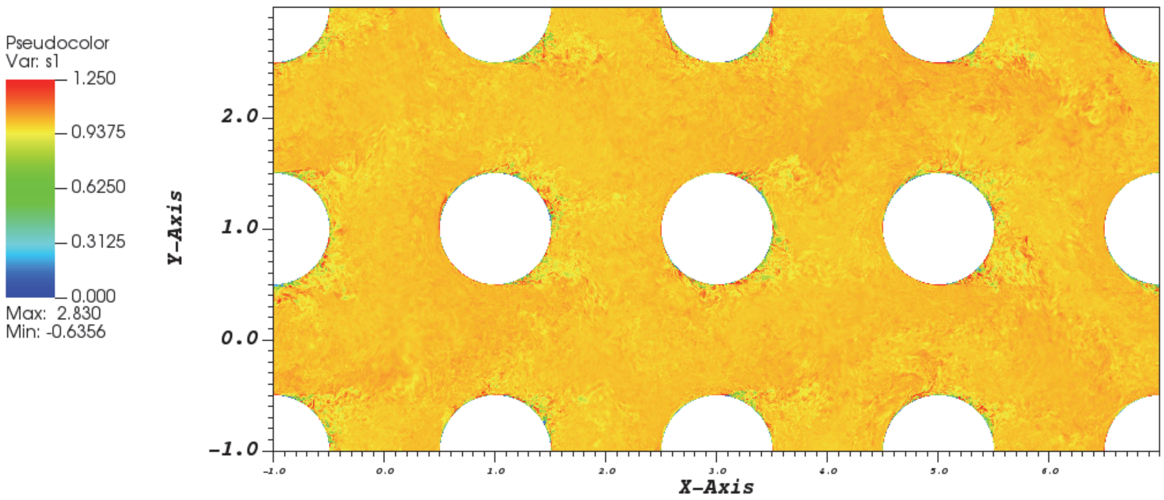

Figure 25 Instantaneous concentration field at Re=16072 Sc=10

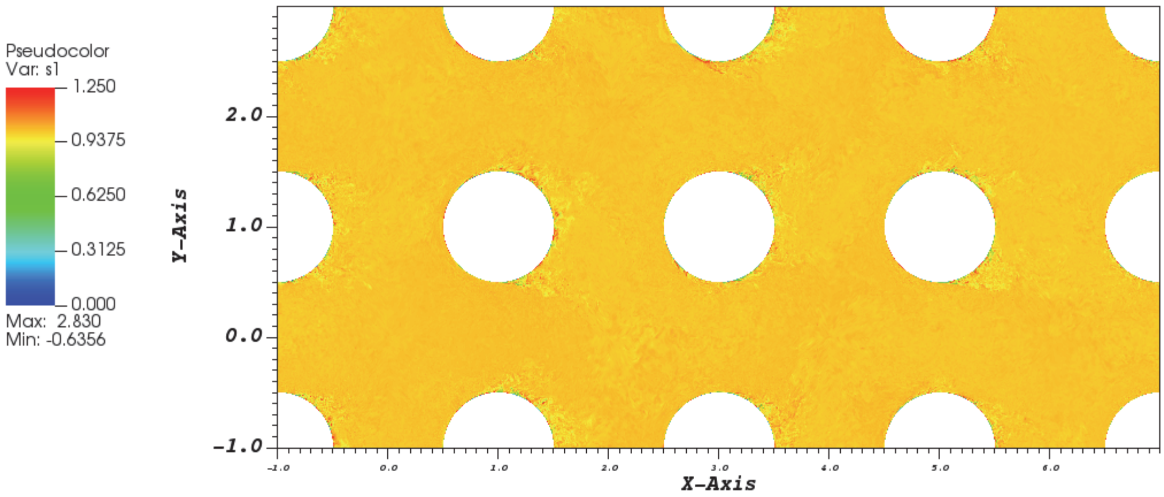

Figure 26 Instantaneous concentration field at Re=16072 Sc=50

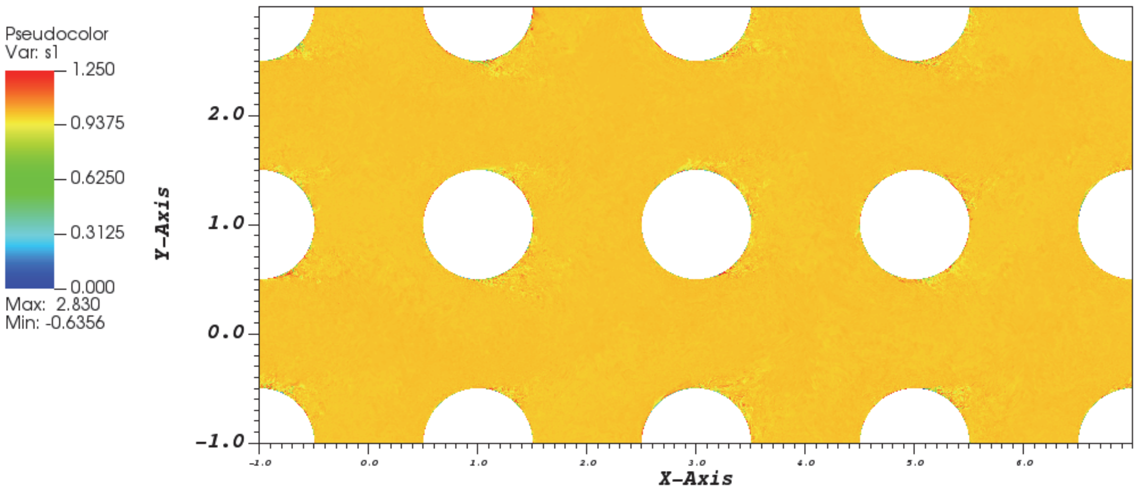

Figure 27 Instantaneous concentration field at Re=16072 Sc=100

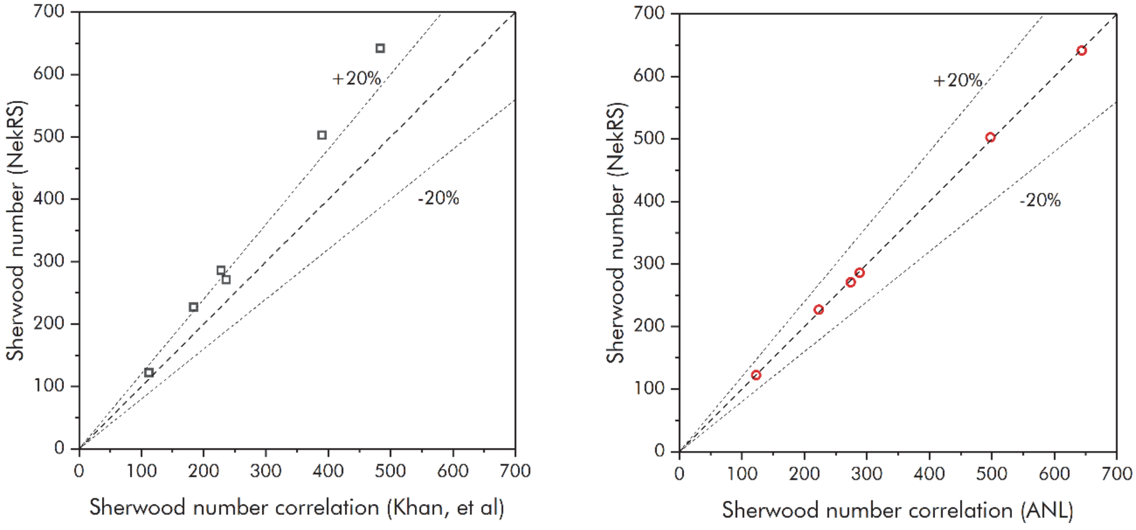

Figure 28 Comparison of Sherwood numbers obtained from NekRS simulations with existing correlation (left) and new correlation (right) for tube bank case

4.3.3 In-line subchannel

The third geometry we considered is that of a reactor core subchannel. The subchannel case used a nondimensional fuel pin diameter of 1.0, with pitch of 1.33 and nondimensional length of 6.0. The numerical domain and cross-sectional mesh are shown in Figure 29 and Figure 30 respectively. The mesh had 102400 elements with polynomial order of seven, leading to more than 35 million total Degrees of Freedom (DOF). Similar to the tube case, we also tested at two *Re* numbers and three *Sc* numbers. Figure 31 shows contours of the instantaneous velocity magnitude field at *Re* = 3750 and 12500 respectively. Figure 32 and Figure 33 presents contours of the instantaneous concentration profile at different *Re* and *Sc*. Greater turbulence character is again observed with increased Re and Sc.

Similar to the previous cases, we could again borrow the heat transfer correlations for in-line subchannels to create an analogous mass transfer correlation [41].

$$Sh = 0.023\ (P/D)\ Re^{0.8}\ Sc^{0.33}$$

The comparison between data from NekRS simulation and the above correlation is demonstrated in Figure 34. Again, the trend is similar both datasets, namely Sherwood number increases with increased Re and Sc. However, this time the correlation substantially underpredicted the mass transfer compared to the simulated values with a mean relative error of 42%. This again indicated significant deficiency in the correlation. Using the NekRS results as the baseline, a more accurate correlation was sought for this geometry. This correlation took the form shown below

$$Sh = 9.6 \times 10^{-4}\ (P/D)\ Re^{1.10}\ Sc^{0.36}$$

A comparison between the new correlation and the simulation results is shown in Figure 23. The new correlation has a mean relative error of only 3%, indicating a much-improved correlation. As such, the new ANL-established correlation will be provided to Mole to account for mass transfer in this geometry.

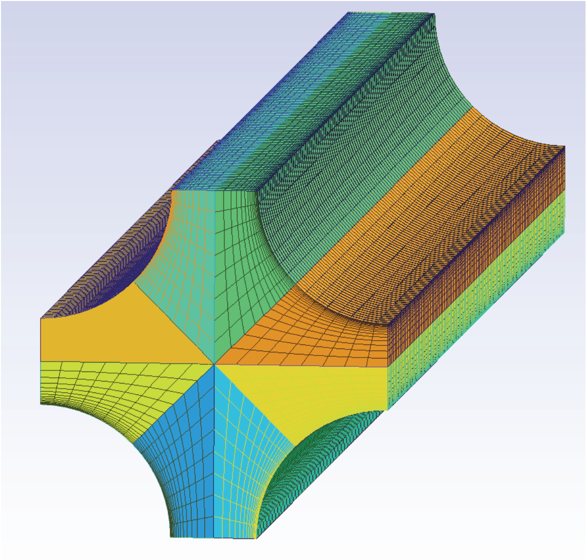

Figure 29 Numerical domain for subchannel case

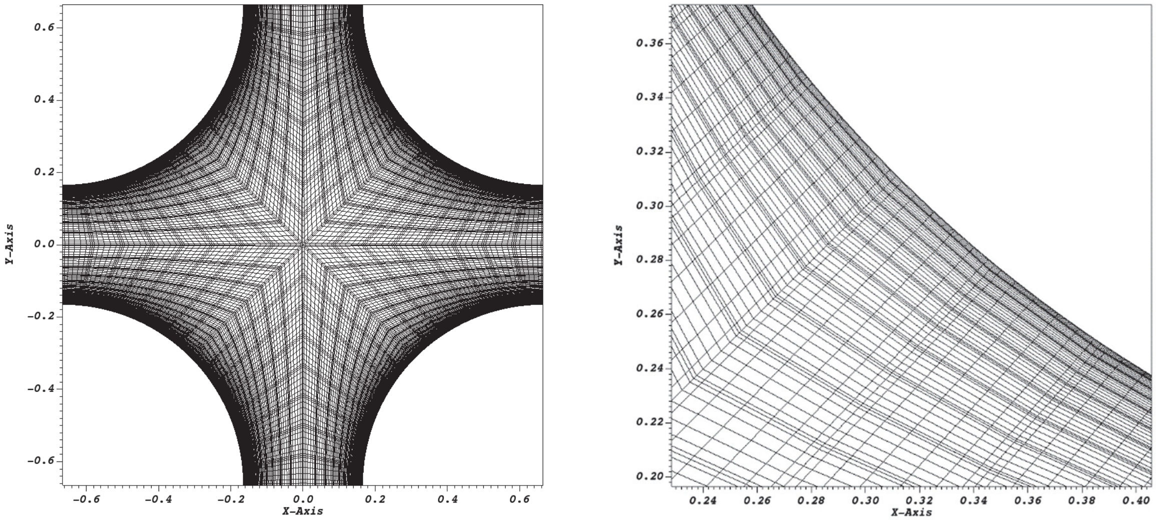

Figure 30 Mesh at cross section of subchannel

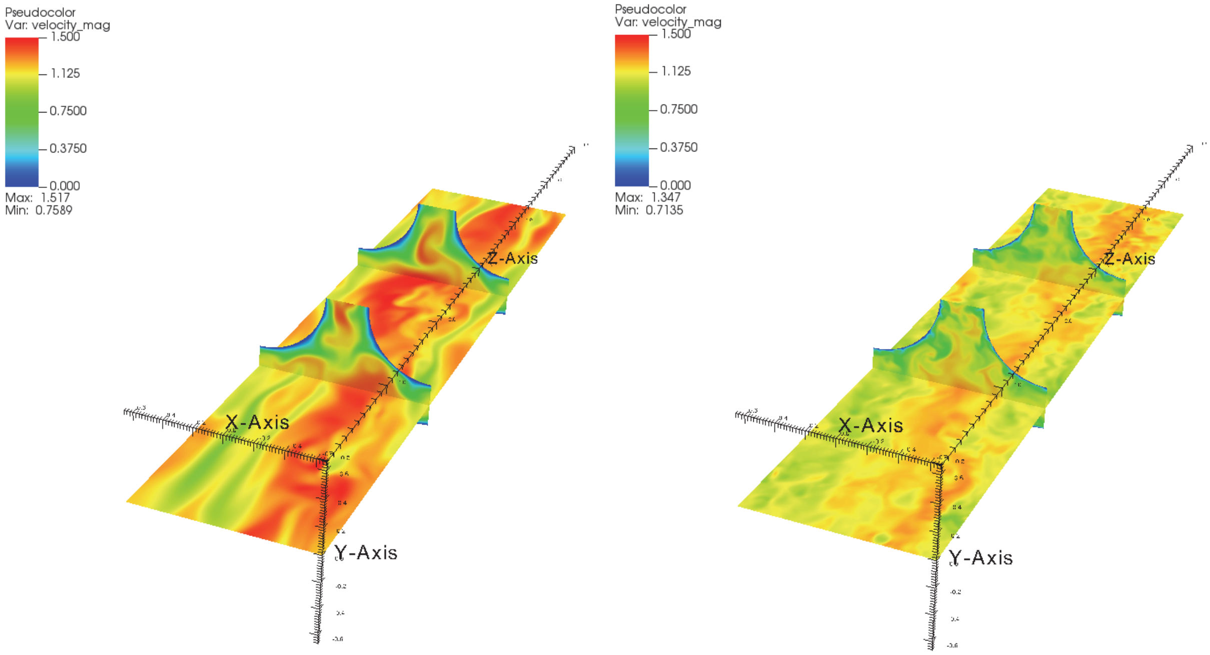

Figure 31 Instantaneous velocity magnitude in subchannel (left: Re=3750, Right: Re=12500)

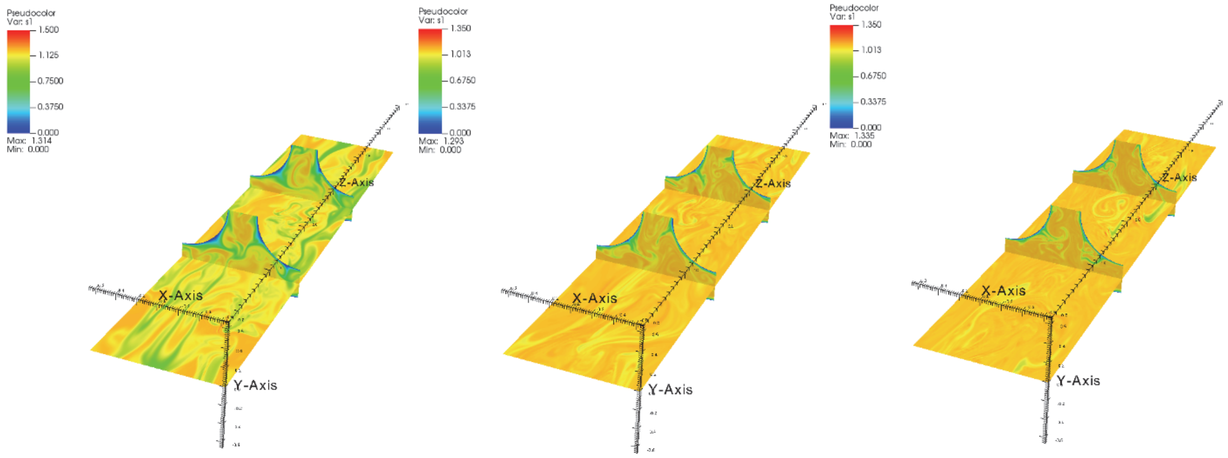

Figure 32 Instantaneous concentration field at Re=3750 (left: Sc=10, middle: Sc=50, right: Sc=100)

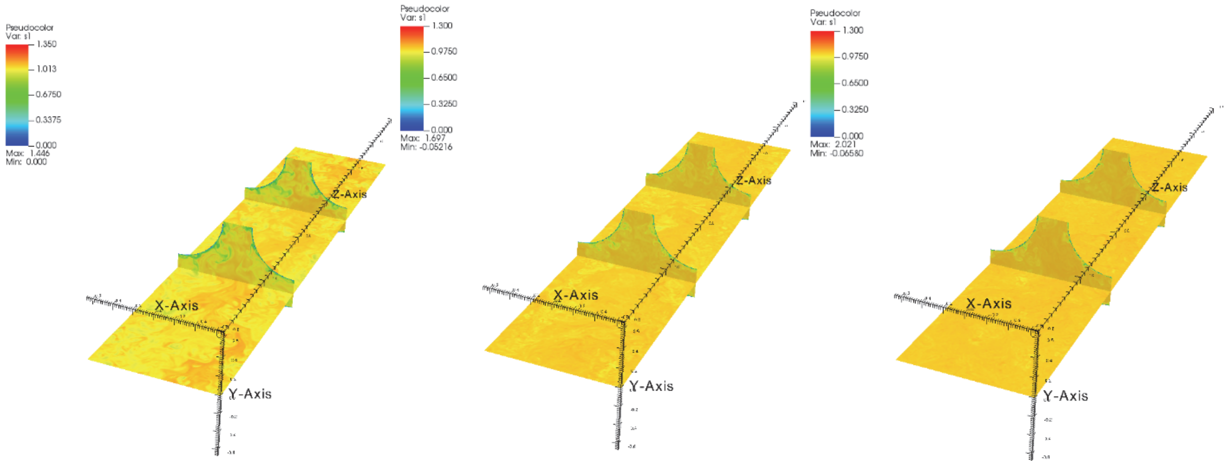

Figure 33 Instantaneous concentration field at Re=12500 (left: Sc=10, middle: Sc=50, right: Sc=100)

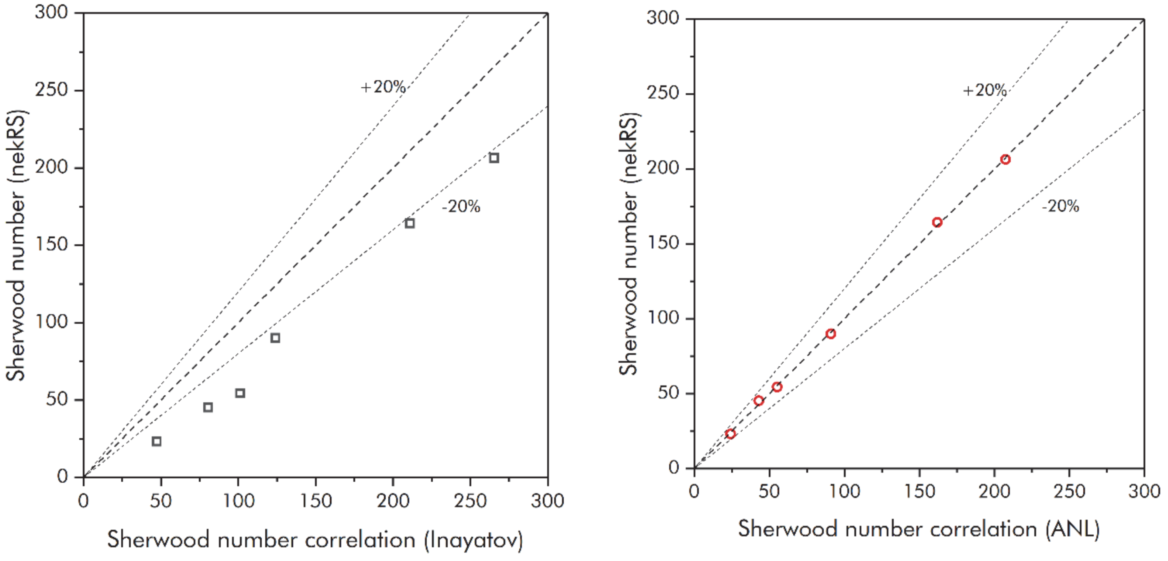

Figure 34 Comparison of Sherwood numbers obtained from NekRS simulations with the existing correlation (left) and the new correlation (right) for the subchannel case

5. Conclusions and Future Work

In this report, we presented the current status of the MOSCATO code package. This solver is capable of high-fidelity simulations of the chemistry and corrosion in molten salt systems. During FY21, the solver was transitioned from OpenFOAM to Nek5000 to provide increased performance and parallelizability. Using the updated code, we were able to simulate several demonstration cases relevant to molten salt corrosion, including a full-scale thermal convection loop simulation. We were also able to generate new mass transfer correlations for tubular, tube bank, and subchannel geometries. These correlations can be readily integrated into reduced-order modeling tools such as ORNL's Mole code.

A variety of work is planned for FY22. First, the solver will be further updated to fully make use of the GPU-accelerated enhancements made possible by NekRS. The Artificial Viscosity Model will also be implemented to account for salts species with very large *Sc*. Next, validation and verification activities will be performed to ensure that the correctness of the solver. Interfacing between MOSCATO and the Molten Salt Thermodynamic Database (MSTDB) and the Molten Salt Thermodynamic Database for Thermophysical Properties (MSTDB-TP) will also be pursued to provide thermodynamic and thermophysical properties values for MOSCATO. Finally, additional high-fidelity chemical engineering correlations will be generated for a variety of MSR-relevant geometries. In completing these tasks, we will develop an advanced, high-performance tool for molten salt chemistry modeling and provide crucial data to enable the success of reduced-order modeling approaches.

Reference

[1] H. G. Macpherson, “The Molten Salt Reactor Adventure,” *Nucl. Sci. Eng.*, vol. 90, no. 4, pp. 374–380, 1985.

[2] J. Serp, M. Allibert, V. Ghetta, D. Heuer, D. Holcomb, V. Ignatiev, J. Leen, L. Luzzi, E. Merle-lucotte, J. Uhlí, and D. Zhimin, “Progress in Nuclear Energy The molten salt reactor (MSR) in generation IV : Overview and perspectives,” *Prog. Nucl. Energy*, vol. 77, pp. 308–319, 2014.

[3] C. W. Forsberg, P. F. Peterson, and P. S. Pickard, “Molten-salt-cooled advanced high-temperature reactor for production of hydrogen and electricity,” *Nucl. Technol.*, vol. 144, no. 3, pp. 289–302, 2003.

[4] Koger J.W., “Chromium Depletion and Void Formation in Fe—Ni—Cr Alloys During Molten Salt Corrosion and Related Processes,” in *Advances in Corrosion Science and Technology*, Springer, Boston, MA., 1974, pp. 245–318.

[5] R. J. Kedl, “THE MIGRATION OF A CLASS OF FISSION PRODUCTS (NOBLE METALS) IN THE MOLTEN-SALT REACTOR EXPERIMENT,” ORNL-TM-3994, Reactor Division, Oak Ridge National Laboratory, 1972.

[6] J. R. Keiser, J. H. DeVan, and D. L. Manning, “The Corrosion Resistance of Type 316 Stainless Steel to Li2BeF4,” ORNL-TM-5782, Metal And Ceramics Division, Oak Ridge National Laboratory, 1977.

[7] J. Newman and K. E. Thomas-Alyea, *Electrochemical Systems*. Hoboken, New Jersy: John Wiley & Sons, 2004.

[8] M. Buoni and L. Petzold, “An efficient , scalable numerical algorithm for the simulation of electrochemical systems on irregular domains,” *J. Comput. Phys.*, vol. 225, no. 2, pp. 2320–2332, 2007.

[9] M. Buoni and L. Petzold, “An algorithm for simulation of electrochemical systems with surface – bulk coupling strategies,” *J. Comput. Phys.*, vol. 229, no. 2, pp. 379–398, 2010.

[10] D. B. Weitzel, “An Experimental and Numerical Investigation of Flow Accelerated FLiBe Corrosion,” Univeristy of New Mexico, 2019.

[11] J. W. Koger, “ALLOY COMPATIBILITY WITH LiF-BeF 2 SALTS CONTAINING

ThF4 AND UF4," ORNL-TM-4286, Metal And Ceramics Division, Oak Ridge National Laboratory, 1972.

[12] H. Yuan and N. Hoyt, "MULTICOMPONENT MASS TRANSFER OF ACTINIDES IN NUCLEAR-RELEVANT MOLTEN SALTS," in *ANS Global and Top Fuel*, 2019.

[13] OpenCFD Limited, "OpenFOAM User Guide," 2011. [Online]. Available: http://www.openfoam.org/docs/user/. [Accessed: 20-Jan-2016].

[14] V. Novaresio, M. García-camprubí, S. Izquierdo, and P. Asinari, "An open-source library for the numerical modeling of mass-transfer in solid oxide fuel cells ☆," *Comput. Phys. Commun.*, vol. 183, no. 1, pp. 125–146, 2012.

[15] Y. Maday, A. T. Patera, and E. M. Rnquist, "An Operator-Integration-Factor Splitting Method for Time-Dependent Problems : Application to Incompressible Fluid Flow," *J. Sci. Comput.*, vol. 5, no. 4, pp. 263–292, 1990.

[16] M. O. Deville, P. F. Fischer, and E. H. Mund, *High-Order Methods for Incompressible Fluid Flow*. Cambridge University Press, 2002.

[17] E. Merzari, P. Fischer, H. Yuan, K. Van Tichelen, S. Keijers, J. De Ridder, J. Degroote, J. Vierendeels, H. Doolaard, V. R. Gopala, and F. Roelofs, "Benchmark Exercise for Fluid Flow Simulations in a Liquid Metal Fast Reactor Fuel Assembly," *Nucl. Eng. Des.*, vol. 298, no. March 2011, pp. 218–228, 2016.

[18] E. Merzari, A. Obabko, P. Fischer, N. Halford, J. Walker, A. Siegel, and Y. Yu, "Large-scale Large Eddy Simulation of Nuclear Reactor Flows : Issues and Perspectives," *Nucl. Eng. Des.*, vol. 312, pp. 86–98, 2017.

[19] J. Walker, E. Merzari, A. Obabko, P. Fischer, and A. Siegel, "Accurate Prediction of the Wall Shear Stress in Rod Bundles with the Spectral Element Method at High Reynolds Numbers," *Int. J. Heat Fluid Flow*, vol. 50, pp. 287–299, 2014.

[20] S. Stolz, P. Schlatter, and L. Kleiser, "High-pass Filtered Eddy-viscosity Models for Large-eddy Simulations of Transitional and Turbulent Flow," *Phys. Fluids*, vol. 17, no. 6, p. 065103, 2005.

[21] P. Schlatter, S. Stolz, and L. Kleiser, "LES of Transitional Flows using the Approximate Deconvolution Model," *Int. J. Heat Fluid Flow*, vol. 25, pp. 549–558, 2004.

[22] P. Fischer, S. Kerkemeier, M. Min, Y.-H. Lan, M. Phillips, T. Rathnayake, E. Merzari, A.

Tomboulides, A. Karakus, N. Chalmers, and T. Warburton, "NekRS, a GPU-Accelerated Spectral Element Navier-Stokes Solver," 2021.

[23] K. Świrydowicz, N. Chalmers, A. Karakus, and T. Warburton, "Acceleration of tensor-product operations for high-order finite element methods," *Int. J. High Perform. Comput. Appl.*, vol. 33, no. 4, pp. 735–757, 2019.

[24] A. Karakus, N. Chalmers, K. Świrydowicz, and T. Warburton, "A GPU accelerated discontinuous Galerkin incompressible flow solver," *J. Comput. Phys.*, vol. 390, pp. 380–404, 2019.

[25] B. Johannesson, "Development of a Generalized Version of the Poisson – Nernst – Planck Equations Using the Hybrid Mixture Theory : Presentation of 2D Numerical Examples," *Transp. Porous Media*, vol. 85, no. 2, pp. 565–592, 2010.

[26] K. Britsch, M. Anderson, P. Brooks, and K. Sridharan, "Natural circulation FLiBe loop overview," *Int. J. Heat Mass Transf.*, vol. 134, pp. 970–983, 2019.

[27] R. R. Romatoski and L. W. Hu, "Fluoride salt coolant properties for nuclear reactor applications : A review," *Ann. Nucl. Energy*, vol. 109, pp. 635–647, 2017.

[28] M. van Reeuwijk and M. Hadžiabdić, "Modelling high Schmidt number turbulent mass transfer," *Int. J. Heat Fluid Flow*, vol. 51, pp. 42–49, 2015.

[29] D. A. Shaw and T. J. Hanratty, "Turbulent mass transfer rates to a wall for large Schmidt numbers," *AIChE J.*, vol. 23, no. 1, pp. 28–37, 1977.

[30] S. W. Churchill, "Comprehensive Correlating Equations for Heat, Mass and Momentum Transfer in Fully Developed Flow in Smooth Tubes," *Ind. Eng. Chem. Fundam.*, vol. 16, no. 1, pp. 109–116, 1977.

[31] S. Aravinth, "Prediction of heat and mass transfer for fully developed turbulent fluid flow through tubes," *Int. J. Heat Mass Transf.*, vol. 43, no. 8, pp. 1399–1408, 2000.

[32] Y. Tominaga and T. Stathopoulos, "Turbulent Schmidt numbers for CFD analysis with various types of flowfield," *Atmos. Environ.*, vol. 41, no. 37, pp. 8091–8099, 2007.

[33] A. N. Colli and J. M. Bisang, "A CFD Study with Analytical and Experimental Validation of Laminar and Turbulent Mass-Transfer in Electrochemical Reactors," *J. Electrochem. Soc.*, vol. 165, no. 2, pp. E81–E88, 2018.

[34] F. Schwertfirm and M. Manhart, “DNS of passive scalar transport in turbulent channel flow at high Schmidt numbers,” *Int. J. Heat Fluid Flow*, vol. 28, no. 6, pp. 1204–1214, 2007.

[35] Y. Hasegawa and N. Kasagi, “Low-pass filtering effects of viscous sublayer on high Schmidt number mass transfer close to a solid wall,” *Int. J. Heat Fluid Flow*, vol. 30, no. 3, pp. 525–533, 2009.

[36] B. M. Mitrovic, P. M. Le, and D. V. Papavassiliou, “On the Prandtl or Schmidt number dependence of the turbulent heat or mass transfer coefficient,” *Chem. Eng. Sci.*, vol. 59, no. 3, pp. 543–555, 2004.

[37] S. B. Pope, *Turbulent Flows*, 8th ed. Cambridge University Press, 2000.

[38] S. . Van Haren, “Testing DNS capability of OpenFOAM and STAR-CCM +,” Delft University of Technology, 2011.

[39] W. V. Pinczewski and S. Sideman, “A model for mass (heat) transfer in turbulent tube flow. Moderate and high schmidt (prandtl) numbers,” *Chem. Eng. Sci.*, vol. 29, no. 9, pp. 1969–1976, 1974.

[40] W. A. Khan, J. R. Culham, and M. M. Yovanovich, “Convection heat transfer from tube banks in crossflow: Analytical approach,” *Int. J. Heat Mass Transf.*, vol. 49, no. 25–26, pp. 4831–4838, 2006.

[41] A. Y. Inayatov, “CORRELATION OF DATA ON HEAT TRANSFER. FLOW PARALLEL TO TUBE BUNDLES AT RELATIVE TUBE RITCHES OF 1.1<S/D<1.6.,” *Heat Transf. - Sov. Res.*, vol. 7, no. 3, pp. 84–88, 1975.

Argonne
NATIONAL LABORATORY

Nuclear Science and Engineering Division
Argonne National Laboratory
9700 South Cass Avenue, Bldg. 208
Argonne, IL 60439

www.anl.gov

U.S. DEPARTMENT OF
ENERGY